

# Making $h(t)$ for Advanced LIGO

Aaron Viets,<sup>1,2</sup> Madeline Wade,<sup>3</sup> Alex Urban,<sup>4</sup> Shivaraj Kandhasamy,<sup>5</sup> Joe Betzwieser,<sup>5</sup> Duncan Brown,<sup>6</sup> Jordi Burguet-Castell, Craig Cahillane,<sup>4</sup> Evan Goetz,<sup>7</sup> Kiwamu Izumi,<sup>7</sup> Sudarshan Karki,<sup>7,8</sup> Jeff Kissel,<sup>7</sup> Greg Mendell,<sup>7</sup> Rick Savage,<sup>7</sup> Xavier Siemens,<sup>1</sup> Darkhan Tuyenbayev,<sup>7,9</sup> Alan Weinstein<sup>4</sup>

<sup>1</sup>*University of Wisconsin-Milwaukee, Milwaukee, WI 53201, USA*

<sup>2</sup>*Concordia University Wisconsin, Mequon, WI 53097, USA*

<sup>3</sup>*Kenyon College, Gambier, OH 43022, USA*

<sup>4</sup>*California Institute of Technology, Pasadena, CA 91125, USA*

<sup>5</sup>*LIGO Livingston Observatory, Livingston, LA 70803, USA*

<sup>6</sup>*Syracuse University, Syracuse, NY 13244, USA*

<sup>7</sup>*LIGO Hanford Observatory, Richland, WA 99352, USA*

<sup>8</sup>*University of Oregon, Eugene, OR 97403, USA*

<sup>9</sup>*University of Texas Rio Grande Valley, Brownsville, TX 78520, USA*

Advanced LIGO’s raw detector output needs to be calibrated to compute dimensionless strain  $h(t)$ . Calibrated gravitational-wave (GW) strain data is produced in the time domain using both a low-latency, online procedure and a high-latency, offline procedure. The low-latency  $h(t)$  data stream is produced in two stages, the first of which is performed on the same computers that operate the detector’s feedback control system. This stage, referred to as the front-end calibration, uses infinite impulse response (IIR) filtering and performs all operations at a 16384 Hz digital sampling rate. Due to several limitations, this procedure currently introduces certain systematic errors in the calibrated strain data, motivating the second stage of the low-latency procedure, known as the low-latency `gstl1al` calibration pipeline. The `gstl1al` calibration pipeline uses finite impulse response (FIR) filtering to apply corrections to the output of the front-end calibration. It applies time-dependent correction factors to the sensing and actuation components of the calibrated strain to reduce systematic errors. The `gstl1al` calibration pipeline is also used in high latency to recalibrate the data, which is necessary due mainly to online dropouts in the calibrated data and identified improvements to the calibration models or filters.

## I. INTRODUCTION

Gravitational waves (GWs) represent a new messenger for astronomy, carrying information about compact objects in the local universe such as neutron stars and black holes. To date, the Laser Interferometer Gravitational-wave Observatory (LIGO) has observed several transient GW signals from merging stellar-mass black hole binaries [1–5] and a double neutron star binary [6], and has recently finished the second Observing Run (O2) of the Advanced LIGO era. There are two LIGO observatories in North America: one in Hanford, WA (H1) and another in Livingston, LA (L1).

Each LIGO detector consists of two orthogonal arms,  $L_x$  and  $L_y$ , roughly 4 km in length (Fig. 1). External gravitational-wave signals are measured from changes in the differential arm (DARM) length,

$$\Delta L_{\text{free}}(t) = \Delta L_x(t) - \Delta L_y(t), \quad (1)$$

between pairs of test masses at opposite ends of  $L_x$  and  $L_y$ . Differential length displacements are measured using interferometric techniques [8]: the test masses consist of highly reflective mirrors that form a pair of resonant Fabry-Pérot cavities. Input laser light passes through a beamsplitter, enters the resonant cavities, then recombines out of phase at an output photodiode. Any power fluctuations measured by the output photodiode will then correspond to differential arm length changes. To further improve sensitivity, a power recycling mirror at the input reflects laser light back into the arms of the interferometer (IFO) to increase the laser power stored in the arms. A signal recycling mirror at the output enhances the IFO sensitivity in the frequency band of interest [9–11].

However, we cannot measure  $\Delta L_{\text{free}}(t)$  directly because the Fabry-Pérot cavities are held in resonance by servos actuating the test masses in response to external stimuli, actively suppressing low-frequency fluctuations in  $\Delta L_{\text{free}}(t)$  [8]. The servos are part of a feedback control system, known as the DARM control loop, whose residual signal, known as the error signal, is our primary observable, and from which any external length disturbance needs to be reconstructed. In practice, this is done by modeling various transfer functions in the DARM control loop, usually with reference measurements taken prior to the start of science-quality observation runs, and then applying them as filters in the time domain [7, 12]. Historically, calibration was originally done in the frequency domain. The idea of producing a more convenient time-domain calibration came from GEO600 and has been employed since Initial LIGO’s second science run [12].

It is also important to note that small variations do occur in the detectors over time due to, for example, drifts in the alignment system. Changes in the calibration over time are generally minor and do not affect the long-term stability of detector operation, but when uncompensated, they do cause systematic biases in the calibrated strain data that can negatively impact estimation of parameters from astrophysical gravitational-wave signals [13]. Fortunately, most variations are small and slow compared to the rapid timescale (16384 Hz) on which we record and analyze data. To a good approximation, we can treat them as either time-dependent gains on DARM loop transfer functions, or changes in the zero or pole frequencies of those transfer functions [7, 14].

A simplified model of the DARM control loop is shown in Fig. 2. Any length disturbances that arise from external

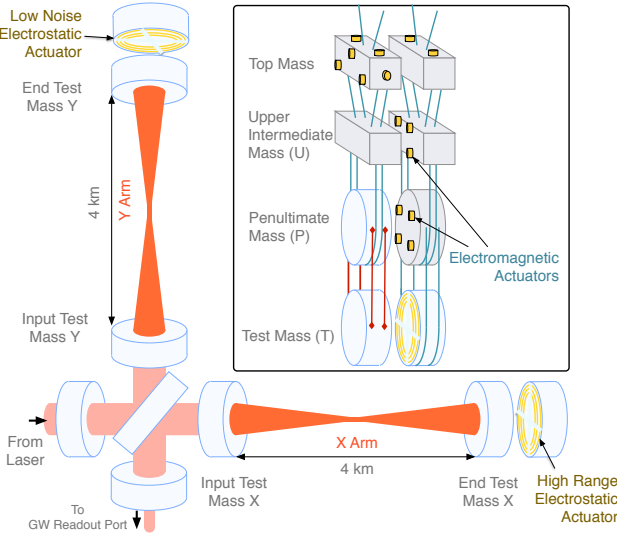


FIG. 1. Simplified diagram of an Advanced LIGO detector. A set of four highly reflective mirrors act as test masses, forming an orthogonal pair of Fabry-Pérot cavities. Laser light enters from the lower left, passes through a beamsplitter, and enters resonant cavities in each 4 km arm. The laser light then recombines out of phase at the gravitational wave output port, which records an error signal used to actuate the end test masses to hold each cavity in resonance. For clarity, only the lowest suspension stage is shown for the optics. *Inset:* an illustration of one of the dual-chain, quadruple pendulum suspension systems with actuators. This figure is reproduced with permission from [7].

sources, including gravitational waves and displacement noise, enter the loop as  $\Delta L_{\text{free}}(t)$ . A controlled length differential,  $\Delta L_{\text{ctrl}}(t)$ , compensates part of this external displacement, giving a residual displacement

$$\Delta L_{\text{res}}(t) = \Delta L_{\text{free}}(t) - \Delta L_{\text{ctrl}}(t). \quad (2)$$

The residual is directly sensed by the detector and read out as an error signal

$$d_{\text{err}}(t) = C * \Delta L_{\text{res}}(t) \quad (3)$$

where  $C$  is a sensing function representing the opto-mechanical response of the IFO to changes in the DARM length. The operation

$$F * g(t) = \int_{-\infty}^{\infty} F(\tau) g(t - \tau) d\tau \quad (4)$$

denotes convolution of some time domain filter  $F$  with some signal  $g(t)$ . As indicated by Eq. (3), our model relies on the linearity of the detector's response, which is enforced by holding the arm cavities slightly off resonance. This is done by digitally adding a very small DC offset, and causes a small amount of light to exit the IFO at the readout port. [15]

The error signal is also used to create a control signal,  $d_{\text{ctrl}}(t)$ . The control signal feeds into the actuation system, which acts

on the suspension pendula to hold the Fabry-Pérot cavities in resonance (Fig. 2). The controlled length differential is

$$\Delta L_{\text{ctrl}}(t) = A * d_{\text{ctrl}}(t) \quad (5)$$

where  $A$  is a filter representing the combined electromechanical actuation response from each pendulum stage. In terms of the observable  $d_{\text{err}}(t)$  and its corollary  $d_{\text{ctrl}}(t)$ , the external length differential is therefore

$$\Delta L_{\text{free}}(t) = C^{-1} * d_{\text{err}}(t) + A * d_{\text{ctrl}}(t) \quad (6)$$

where  $C^{-1}$  is the filter inverse of  $C$ .

The external length differential can also be computed from solely the error signal. Historically, we have used both the error and control signals [12], as shown in Eq. (6), for two main reasons. First, this allows the computation of  $\Delta L_{\text{free}}(t)$  to be insensitive to the digital filters  $D$ , which are often changed to improve the control loop design.<sup>1</sup> Second, the predetermined control signal  $x_{\text{ctrl}}(t)$ , shown in Fig. 2, will not appear in the resulting  $\Delta L_{\text{free}}(t)$  spectrum due to its location in the feedback loop between the  $d_{\text{err}}(t)$  and  $d_{\text{ctrl}}(t)$  pickoff points.

The dimensionless strain  $h(t)$  used for detecting gravitational waves is a time series derived from  $\Delta L_{\text{free}}(t)$ ,

$$h(t) = \frac{\Delta L_{\text{free}}(t)}{L}, \quad (7)$$

where  $L = (L_x + L_y)/2$  is the average measured arm length. Since fluctuations in  $L$  are negligible, the process of calibration therefore amounts to reconstructing  $\Delta L_{\text{free}}(t)$  from  $d_{\text{err}}(t)$  and  $d_{\text{ctrl}}(t)$ . Hereafter we will use  $\Delta L_{\text{free}}(t)$  or  $h(t)$  interchangeably to refer to the final calibrated data product.

Eq. (6) establishes a method for producing calibrated strain data from the error and control signals. We need only to construct accurate physical models for the filters  $C^{-1}$  and  $A$  (then divide by a measurement of  $L$ , which does not change). In Sec. II, we outline the important physical properties of transfer functions associated with these filters and describe how we correct for small variations over time. All inverse sensing and actuation transfer functions are plotted in Fig. 3, and the impact of slow detector variations on calibration accuracy over time is visualized in Fig. 4. A detailed discussion of the full interferometric response, including its effect on calibration uncertainty, can be found elsewhere [7, 13, 14]. In Sec. III, we describe the pipelines used to perform the calibration in Advanced LIGO's first and second observing runs, and in Sec. IV we conclude.

## II. FREQUENCY DOMAIN MODELS

### A. Sensing Function

After  $\Delta L_{\text{ctrl}}$  is subtracted from  $\Delta L_{\text{free}}$ , the sensing function  $C$  converts any residual test mass displacement  $\Delta L_{\text{res}}$  into a

<sup>1</sup> Now that time dependent correction factors are included in the calibration process, this is actually no longer true. However, it remains a historical motivation for how methods were developed.

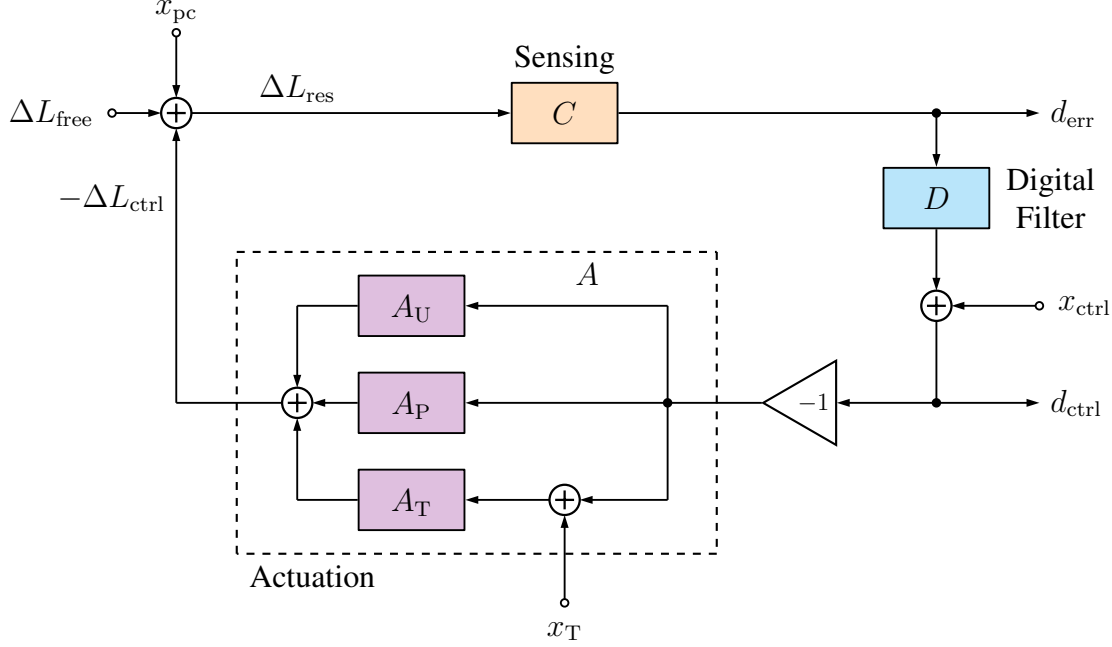


FIG. 2. Block diagram of the Advanced LIGO differential arm (DARM) length feedback control loop. Here, the filter  $C$  is a sensing function representing the IFO's response to changes in the measured differential arm length;  $D$  is a digital control filter; and the filters  $A_U$ ,  $A_P$  and  $A_T$  represent actuation force-to-length responses for the upper-intermediate (U), penultimate (P) and test mass (T) stages of LIGO's quadrupole pendulum suspension system. Length disturbances from external sources, including gravitational waves, enter the loop as  $\Delta L_{\text{free}}$ . The controlled length,  $\Delta L_{\text{ctrl}}$ , is subtracted from this to give a length change residual,  $\Delta L_{\text{res}}$ , which passes through the sensing function resulting in a digital error signal,  $d_{\text{err}}$ . The error signal is then filtered through a set of digital filters  $D$  to create a digital control signal,  $d_{\text{ctrl}}$ . The digital filter  $D$  is a linear combination of a low-pass filter and notch filters that prevent excitation of resonances in the test mass suspensions, among other things. The digital control signal  $d_{\text{ctrl}}$  is used to actuate against the suspension pendula to hold the optical cavities in resonance. Calibration of Advanced LIGO strain data consists of reconstructing  $\Delta L_{\text{free}}$  from  $d_{\text{err}}$ ,  $d_{\text{ctrl}}$  and models of the filters  $C^{-1}$  and  $A = A_U + A_P + A_T$ . Lastly, to check accuracy and precision we inject known sinusoidal excitations (i.e. calibration lines) at three points in the loop, represented by  $x_{\text{pc}}$  (injected through radiation pressure by a small laser),  $x_{\text{ctrl}}$  (injected into the control signal), and  $x_T$  (injected into the test mass actuation stage).

digitized error signal representing the remaining fluctuations in laser power at the output photodiode. This signal is measured as  $d_{\text{err}}$  at the gravitational-wave readout port (Fig. 1) with a sample rate of 16384 Hz. The sensing function also accounts for responses of photodiodes and their analog electronics, light-travel time through the Fabry-Pérot cavities, and digitization effects.

A standard suite of calibration measurements, as discussed in [7, 16], informs a static reference model for the sensing function. The static reference model is represented by

$$\tilde{C}^{\text{static}}(f) = \left( \frac{H_C}{1 + if/f_{\text{cc}}} \right) \times \left( \frac{f^2}{f^2 + f_s^2 - if f_s/Q} \right) \times C_R(f) \exp[-2\pi if\tau_C], \quad (8)$$

where the tilde denotes Fourier transformation into the frequency domain. The gain  $H_C$  gives the number of digital counts in  $d_{\text{err}}$  per unit differential length change, in meters. The pole  $f_{\text{cc}}$  is called the coupled cavity pole frequency; it represents the characteristic frequency beyond which the detector response to gravitational waves is significantly attenuated

due to finite average photon storage time in the Fabry-Pérot cavities. Both LIGO interferometers are designed to have the same coupled cavity pole frequency, but in fact their exact values differ because of losses in the optical cavities: during O2, the model reference values were  $f_{\text{cc}} = 360.0$  Hz at H1 and  $f_{\text{cc}} = 376.0$  Hz at L1. The optical spring frequency of the signal recycling cavity (SRC) is represented by  $f_s$  and the quality factor of the SRC is represented by  $Q$ . The next parameter in Eq. (8),  $\tau_C$ , combines computational delay in acquiring the digital signal, a further delay necessary to approximate the majority of the detector response with a single pole, and the light-travel time across the length of each arm. The last factor,  $C_R(f)$ , encodes the remaining frequency dependence above  $\sim 1$  kHz due to photodiode electronics and analog and digital signal processing filters. All parameters are measured before the start of data collection by actuating the test masses with a swept-sine signal, injected through a combination of the signals  $x_{\text{pc}}$ ,  $x_{\text{ctrl}}$ , and  $x_T$ , shown in Fig 2. These measurements are taken roughly once every few months and form a reference model for the full calibration [7].

However, parameters of the sensing function have been found to vary slowly with time. Specifically, the gain  $H_C$ ,

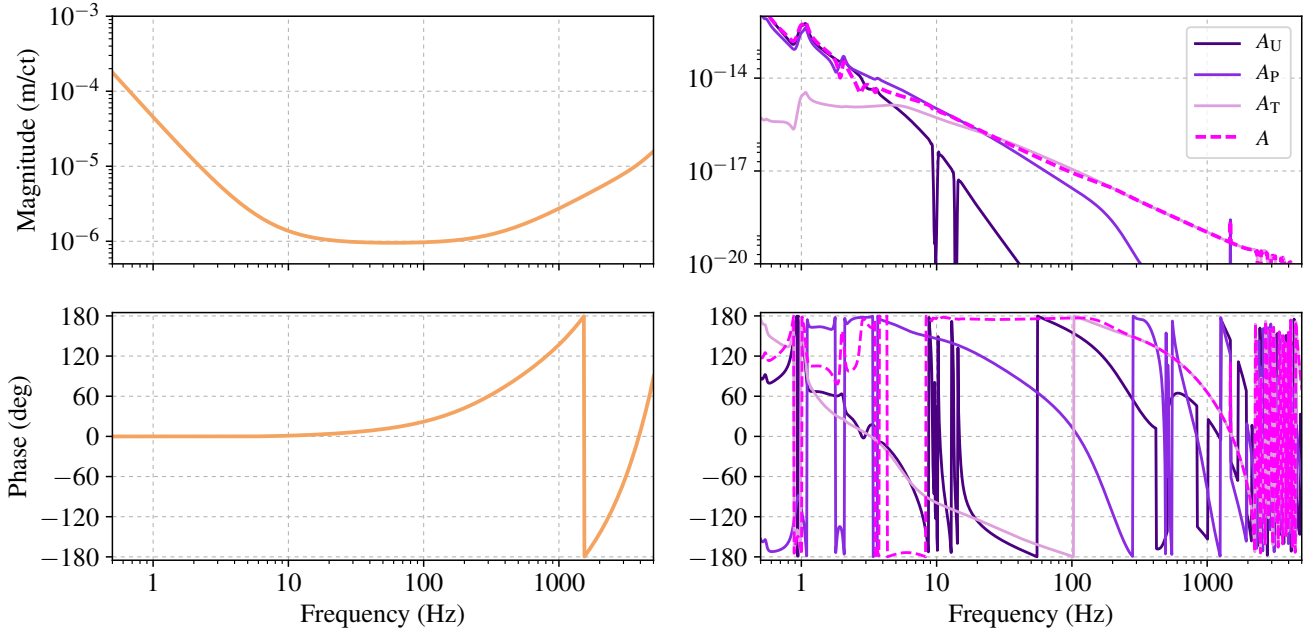


FIG. 3. Frequency-domain models corresponding to the inverse sensing ( $C^{-1}$ , left) and actuation (right) transfer functions as measured at LIGO Hanford Observatory (H1). The inverse sensing function converts  $d_{\text{err}}$  counts to residual displacement, while the actuation function converts  $d_{\text{ctrl}}$  counts to controlled displacement. Note, the factor of  $\sim 10^9$  difference between inverse sensing and total actuation around 10 Hz is due to a very large gain applied to  $d_{\text{err}}$  to create  $d_{\text{ctrl}}$ . At low frequency the inverse sensing is dominated by a low-pass filter around 8 Hz, while above  $\sim 340$  Hz it is affected by  $f_{\text{cc}}$  and above  $\sim 1$  kHz by analog-to-digital conversion. In the actuation response, there are several notch filters used to avoid mechanical resonances. Above  $\sim 30$  Hz, only the test mass stage (T) is actuated against. The corresponding curves at LIGO Livingston Observatory (L1) are qualitatively similar, but differ slightly in scale and frequency dependence; see e.g. [7].

the coupled cavity pole frequency  $f_{\text{cc}}$ , the spring frequency  $f_s$ , and the quality factor of the signal recycling cavity  $Q$  vary with time, as will be discussed in more detail in Sec. II C. The full time-dependent sensing function model is

$$\tilde{C}(f; t) = \kappa_C(t) \left( \frac{H_C}{1 + if/f_{\text{cc}}(t)} \right) \times \left( \frac{f^2}{f^2 + f_s(t)^2 - if f_s(t)/Q(t)} \right) \times C_R(f) \exp[-2\pi if\tau_C]. \quad (9)$$

Variations in the gain  $H_C$  due to changes in laser power and alignment are captured by the factor  $\kappa_C(t)$ , which is set to a value of 1 in the reference model and fluctuates at the level of  $< 10\%$  over time. The time-varying factors in Eq. (9),  $\kappa_C$ ,  $f_{\text{cc}}$ ,  $f_s$ , and  $Q$ , are tracked over time using known sinusoidal excitations (i.e. calibration lines) as described below and in [14, 16]. These factors are all found to change very slowly ( $\sim$  minutes) compared to the timescale of recording data ( $\sim 10^{-4}$  s).

The reference model for  $C^{-1}$ , which converts laser fluctuations back to residual test mass displacement and is represented in the frequency domain by  $1/\tilde{C}^{\text{static}}(f)$ , is plotted in Fig. 3.

## B. Actuation Function

The differential arm length is controlled using electromagnetic actuators on the top three pendulum stages and an electrostatic drive (ESD) actuator on the bottom stage (Fig. 1). While the topmost stage is connected to a seismic isolation system, its actuation strength is relatively small in the Advanced LIGO sensitive frequency band, and the DARM feedback controls are not sent to this topmost stage. The lowest three stages – referred to as the upper intermediate (U), penultimate (P), and test (T) mass stages – are dominant above 10 Hz, and all these stages are displaced in concert [17–20]. The control signal ( $d_{\text{ctrl}}$ ) is distributed to each stage in parallel, converted from digital counts to force, and used to actuate against the mass at that stage. The net result of this is the controlled length differential,  $\Delta L_{\text{ctrl}}$  (Fig. 2).

As with the sensing function, calibration measurements inform a static model for the actuation function. The static reference model for the actuation is represented by a counts-to-length transfer function,

$$\tilde{A}^{\text{static}}(f) = [\tilde{A}_U(f) + \tilde{A}_P(f) + \tilde{A}_T(f)] \exp[-2\pi if\tau_A] \quad (10)$$

where  $\tilde{A}_i(f)$  represent the frequency response of the  $i$ th suspension stage actuator. Filtering that converts digital counts to actuation strength and splits the frequency content of  $d_{\text{ctrl}}$  across each stage of the actuation is folded into these functions

for brevity. The low frequency content of  $d_{\text{ctrl}}$  is directed to the higher stages of the actuation system and the high frequency content is directed to the lower stages. The computational time delay  $\tau_A$  accounts for digital-to-analog conversion. The modeled actuation transfer functions are plotted in Fig. 3.

The actuation function has also been found to have time-dependent gains for each stage of the actuation. The fully time-dependent actuation function model is

$$\tilde{A}(f; t) = [\kappa_U(t)\tilde{A}_U(f) + \kappa_P(t)\tilde{A}_P(f) + \kappa_T(t)\tilde{A}_T(f)] \times \exp[-2\pi if\tau_A] \quad (11)$$

The gains  $\kappa_U(t)$ ,  $\kappa_P(t)$ , and  $\kappa_T(t)$  represent slowly-varying scalar fluctuations over time, due to instrumental artifacts such as charge buildup in the electrostatic drives over time. Changes are typically at the level of a few percent in magnitude, and as with  $\kappa_C(t)$  they can all be tracked and compensated for using injected calibration lines [14].  $\kappa_T$  represents the time-dependence of the electrostatic drive at the test stage of the actuation. The effect of  $\kappa_P$  and  $\kappa_U$  has so far only been tracked as a combined effect  $\kappa_{PU}$ . These normally vary on timescales of hours.

### C. Tracking and Compensating for Small Variations

While in Initial LIGO the only time-dependent correction to the calibration that required tracking and compensation was the gain of the sensing function [12], the situation has become more complex with the Advanced LIGO detectors. The time-dependent correction factors (TDCFs) for the current instruments include  $\kappa_C$ ,  $f_{\text{cc}}$ ,  $\kappa_T$ , and  $\kappa_{PU}$ . These are measured by injecting known sinusoidal excitations (i.e. calibration lines) and tracking their amplitude and phase in  $d_{\text{err}}$  over time. In the H1 detector, the optical spring frequency  $f_s$  and quality factor  $Q$  of the SRC are tracked in a similar manner. Due to their negligible impact in the relevant frequency band in L1, where  $f_s \approx 3$  Hz, the time-dependence of SRC detuning parameters is not currently tracked there.

While the line placement varies in frequency at H1 compared to L1, calibration lines at both detectors serve similar purposes. One such line at frequency  $f_{\text{ctrl}}$  is added to the control signal through  $x_{\text{ctrl}}$  and distributed to each of the lowest three stages in the quadruple pendulum; another at frequency  $f_T$  is injected through  $x_T$  into only the test mass suspension stage; and three (four at H1) at frequencies  $f_i^{\text{pc}}$  are injected through radiation pressure to the end test mass using an additional laser known as a photon calibrator ( $x_{\text{pc}}$ ; Karki *et al.* 16). Length excitations due to all injected signals are suppressed by the DARM control loop, and their influence on  $d_{\text{err}}$  can be predicted with models for  $C$ ,  $D$ , and  $A$ . Appendix A discusses how each TDCF is computed using the calibration lines. A more in-depth discussion can be found in [14].

Fig. 2 shows the injection point of each calibration line. Calibration lines injected using the ESD or the photon calibrator can be seen in the  $h(t)$  spectrum (see Fig. 9). The DARM line,  $x_{\text{ctrl}}$ , does not appear in  $h(t)$  due to the location where it is injected, before  $d_{\text{ctrl}}$  is read out.

A visualization of each calibration line and the effect of correcting for small detector variations is shown in Fig. 4. The data shown are taken from the L1 detector over a period of 72 hours surrounding binary black hole merger GW170104 [4]. Consecutive, non-overlapping Fourier transforms were used to compute strain data in the frequency domain, with integration time of 100 seconds to average out any transient GW signals and to give a frequency resolution of 0.01 Hz. Without compensating for time variations, there can be up to a 15% systematic error in magnitude (and 1-4° systematic error in phase) across Advanced LIGO’s sensitive frequency range, which can impact parameter estimation [3, 21–30]. However, improved calibration is obtained by compensating for these time-varying parameters in the calibration. As with taking reference measurements of the sensing and actuation functions, accurate tracking of the TDCFs during observation relies on the accuracy of the photon calibrator, which has an associated systematic uncertainty of 0.75 % [16].

Having sketched the computations required for precise calibration, we now describe how it is implemented in Advanced LIGO.

## III. CALIBRATION PIPELINES

Low-latency data collection, precise calibration, and analysis are essential for the era of gravitational-wave astronomy, including prompt electromagnetic follow-up of gravitational-wave candidates [31]. Calibration is performed in low latency using a combination of calibration software written for the computers that control the instrument feedback loops, known as the front-end calibration pipeline, and a GStreamer-based [32] pipeline, known as the `gstlal` calibration pipeline. Each of these pipelines will be discussed in detail in Secs. III A and III B.

The front-end calibration pipeline has the advantage of being directly hooked into all of the other front-end computer systems, thereby allowing seamless access to all of the appropriate instrument models and parameters. This enables the calibration model to remain up-to-date and in-sync with the instrument. However, the front-end calibration infrastructure is limited by two features common to real-time computer systems. Originally only delays that are an integer number of digital sampling time intervals (61  $\mu$ s) could be easily implemented using the front-end system. This hurdle, however, has been overcome and will be discussed more below. Additionally, super-Nyquist poles cannot be easily modeled in the front-end calibration. These limitations result in the front-end calibration pipeline introducing about a 5% error in the magnitude of the final strain product.

In order to correct for the shortfalls of the current front-end calibration procedure, the front-end calibration is picked off and fed into a second low-latency calibration pipeline. This second pipeline operates outside of the front-end computers on a set of machines that cannot directly control the interferometer but do receive the data produced by front-end computers in very low latency, within about one second of data collection. The software package used for this second low-latency

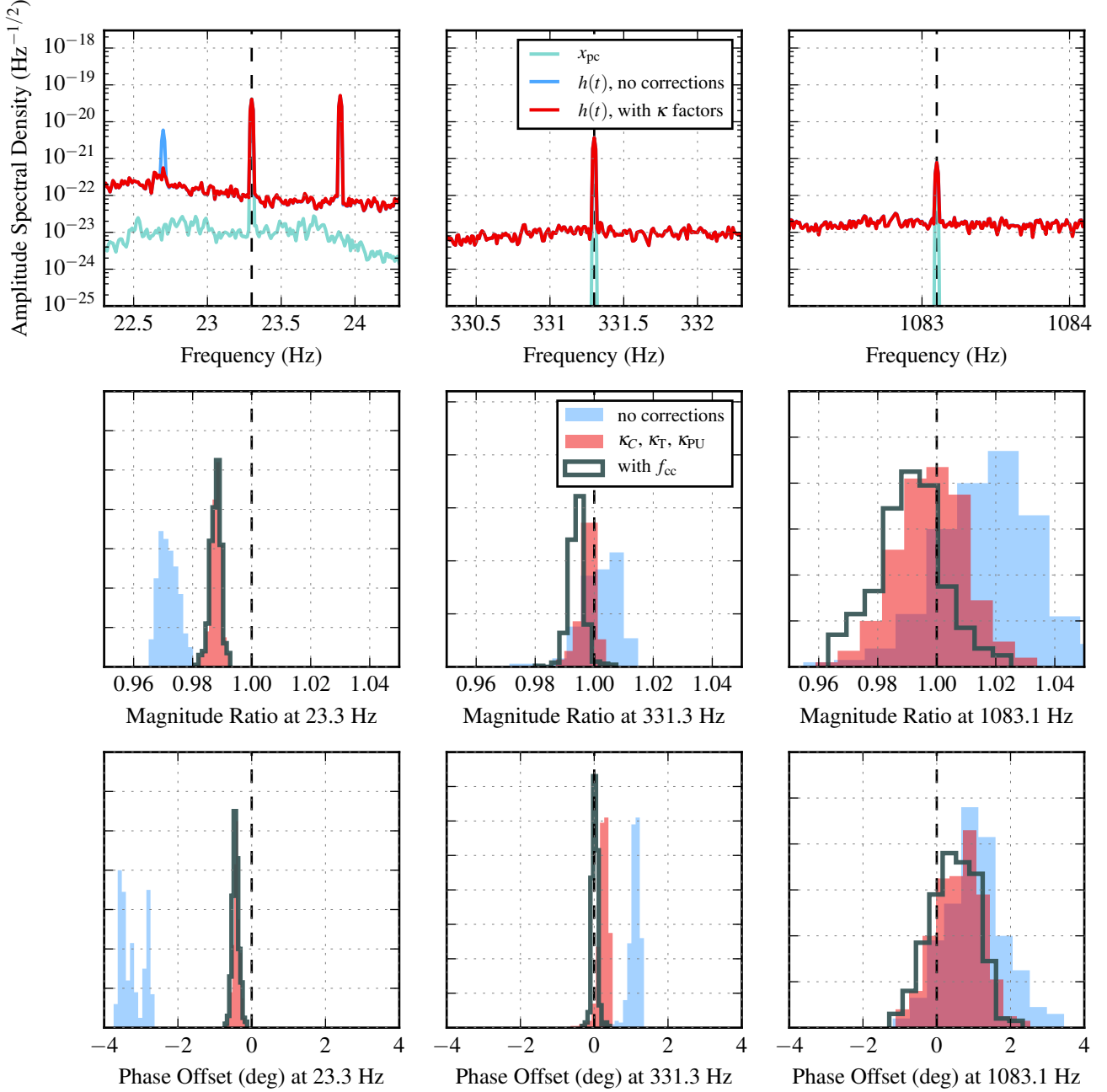


FIG. 4. Impact on calibration accuracy from small deviations in the L1 detector over time. These deviations are quantified by scalar time-dependent factors  $\kappa_C(t)$ ,  $\kappa_T(t)$ , and  $\kappa_{PU}(t)$ , which are applied to the time domain inverse sensing and actuation filters. In addition, the time-dependence of the coupled cavity pole frequency  $f_{cc}$  is tracked but not compensated. In the H1 detector, the optical spring frequency  $f_s$  and quality factor  $Q$  of the signal recycling cavity are also tracked but not compensated. *Top:* A visualization of calibration lines injected into  $h(t)$ . Three of these lines – which live at low, mid and high frequencies, respectively – are injected through radiation pressure against the y-end test mass ( $x_{pc}$ ). *Middle:* Histograms of the magnitude ratio  $|\tilde{h}(f)|/|\tilde{x}_{pc}(f)|$ , measured in the frequency domain at each  $x_{pc}$  line. A series of 100-second Fourier transforms of  $h(t)$  and  $x_{pc}(t)$  were computed covering 72 hours of L1 data surrounding the binary black hole merger signal GW170104 [4]. Note that uncorrected strain contains 1-2% systematic errors in magnitude at all three  $x_{pc}$  lines, which is addressed by compensating for TDCFs. The scale of random errors in these measurements is set by the signal-to-noise ratio of the injected signal. However, correcting for  $f_{cc}$  would introduce an overall  $\sim 1\%$  magnitude offset at mid and high frequencies due to systematics in the measurement of the sensing and actuation functions [13]. *Bottom:* Histograms of the phase offset between  $\tilde{x}_{pc}$  and  $\tilde{h}$  at each  $x_{pc}$  line over the same period. Note that correcting for TDCFs and  $f_{cc}$  completely removes the systematic error in phase at 331.3 Hz, which is in Advanced LIGO's most sensitive band. Results from H1 are similar, although its calibration lines are at slightly different frequencies. During Advanced LIGO's second observing run (O2) there was also a larger variation in  $f_{cc}$  at H1 compared to L1.

TABLE I. Summary of the significant differences and inherent purpose of the different calibration pipelines.

Pipeline	Latency	Accuracy	Input	Type of filtering	Purpose
front-end (0)	real-time	low	$d_{\text{err}}$ and $d_{\text{ctrl}}$	IIR	immediate commissioning feedback
low-latency <code>gstlal</code> (1)	$O(10 \text{ s})$	medium	output of front-end ( $\Delta L_{\text{res}}^0$ and $\Delta L_{\text{ctrl}}^0$ )	FIR	low-latency searches
high-latency <code>gstlal</code> (2)	$O(\text{weeks})$	high	$d_{\text{err}}$ and $d_{\text{ctrl}}$	FIR	final science results

calibration pipeline is `gstlal`, a package that wraps LIGO Algorithm Library (LAL) software [33] with the audio/video streaming software package GStreamer [32, 34]. The low-latency `gstlal` calibration pipeline has an improved latency of about 5-9 seconds in the second observing run. The latency in the first observing run was approximately 10-14 seconds. Since the front-end output is produced in real time, the total latency for the low-latency calibration process is about 5-9 seconds for the second observing run. The `gstlal` calibration pipeline applies high-frequency corrections that could not be applied in the front-end calibration, applies the appropriate time delay to each component of the calibration, and computes a state vector that records the integrity of the final calibration product,  $h(t)$ .

Additionally, there is often a need to recalibrate the data at a later point in time. The most common reasons for recalibrating the data are dropouts of data somewhere in the low-latency system and improved models for the calibration developed over time. The high-latency, offline calibration is therefore the most accurate calibrated strain data produced for Advanced LIGO. The same `gstlal` calibration pipeline is also used for the offline calibration. However, when recalibrating the data offline, the `gstlal` calibration pipeline uses  $d_{\text{err}}$  and  $d_{\text{ctrl}}$  as described in Eq. (6), rather than correcting output of the front-end calibration procedure.

Table I summarizes the differences between each calibration pipeline. The following sections will describe each step of the low- and high-latency calibration procedures.

*Notation:* Throughout the following sections, quantities computed by the front-end calibration pipeline will be denoted with a superscript 0, quantities computed by the low-latency `gstlal` calibration pipeline will be denoted with a superscript 1, and quantities computed by the high-latency `gstlal` calibration pipeline will be denoted with a superscript 2. This notation also distinguishes the filters used in each pipeline. For example,  $C^0$  is the sensing function IIR filter used in the front-end calibration pipeline and  $C^2$  is the sensing function FIR filter used in the high-latency `gstlal` calibration pipeline.

### A. The Front-End Calibration Pipeline

As indicated by Eq. (2), the desired external disturbance  $\Delta L_{\text{free}}$  is obtained by adding the residual error displacement  $\Delta L_{\text{res}}$  and the controlled length differential  $\Delta L_{\text{ctrl}}$ . However, for ease of operation, only the uncalibrated sensing ( $d_{\text{err}}$ ) and control ( $d_{\text{ctrl}}$ ) signals are used in interferometric control loops. The function of the front-end calibration model is to pick off the signals  $d_{\text{err}}$  and  $d_{\text{ctrl}}$  and use Eqs. (3) and (5) to calculate

$$\Delta L_{\text{res}}^0 \text{ and } \Delta L_{\text{ctrl}}^0.$$

#### 1. IIR filters

The front-end calibration pipeline uses infinite impulse response (IIR) filtering techniques. Each component of the static reference models for the inverse sensing function and the actuation function are modeled using zero-pole-gain or second-order section IIR filters. Since it is hard to fit the transfer function measurements with just zero-pole-gain or second-order-section models, these filters introduce systematic errors in the calibrated data at the level of about 1-10%. These systematic errors are later corrected by the `gstlal` calibration pipeline as described in Sec. III B.

The IIR filters used for the actuation function are exact copies of the digital IIR filters used in the actuation path for interferometer controls whenever possible. The full suspension model is simplified, reducing the Q factor of some resonances while removing other high-frequency resonances, such as violin modes, before converting from a continuous representation to a discrete, IIR filter representation. The inverse sensing function is modeled using a single zero, a DC gain, and a high-frequency roll-off. In order to convert from the continuous representation of the actuation and inverse sensing functions to the discrete, IIR filter representation, we use several built-in MATLAB functions, such as `c2d` with the bilinear (Tustin) method [35] and `minreal`, which removes very close zero/pole pairs [36].

High-frequency effects in the actuation and inverse sensing paths are not replicated in the front-end calibration pipeline. We do not attempt to correct high-frequency effects in the actuation path using the `gstlal` calibration pipeline, because the actuation function only contributes to the calibration at low frequencies. However, we do correct the inverse sensing path for high-frequency effects using the `gstlal` calibration pipeline.

#### 2. Front-end calibration pipeline overview

The outputs of the front-end calibration pipeline are the partially calibrated residual signal  $\Delta L_{\text{res}}^0$  and the partially calibrated control signals  $\Delta L_{\text{U}}^0$ ,  $\Delta L_{\text{P}}^0$ , and  $\Delta L_{\text{T}}^0$ , where the combined partially calibrated control signal is  $\Delta L_{\text{ctrl}}^0 = \Delta L_{\text{U}}^0 + \Delta L_{\text{P}}^0 + \Delta L_{\text{T}}^0$ . The fully calibrated output of the front-end calibration is  $\Delta L_{\text{free}}^0$ . Here we outline the basic steps involved in computing each of these outputs, and these steps are shown pictorially in Fig. 5.

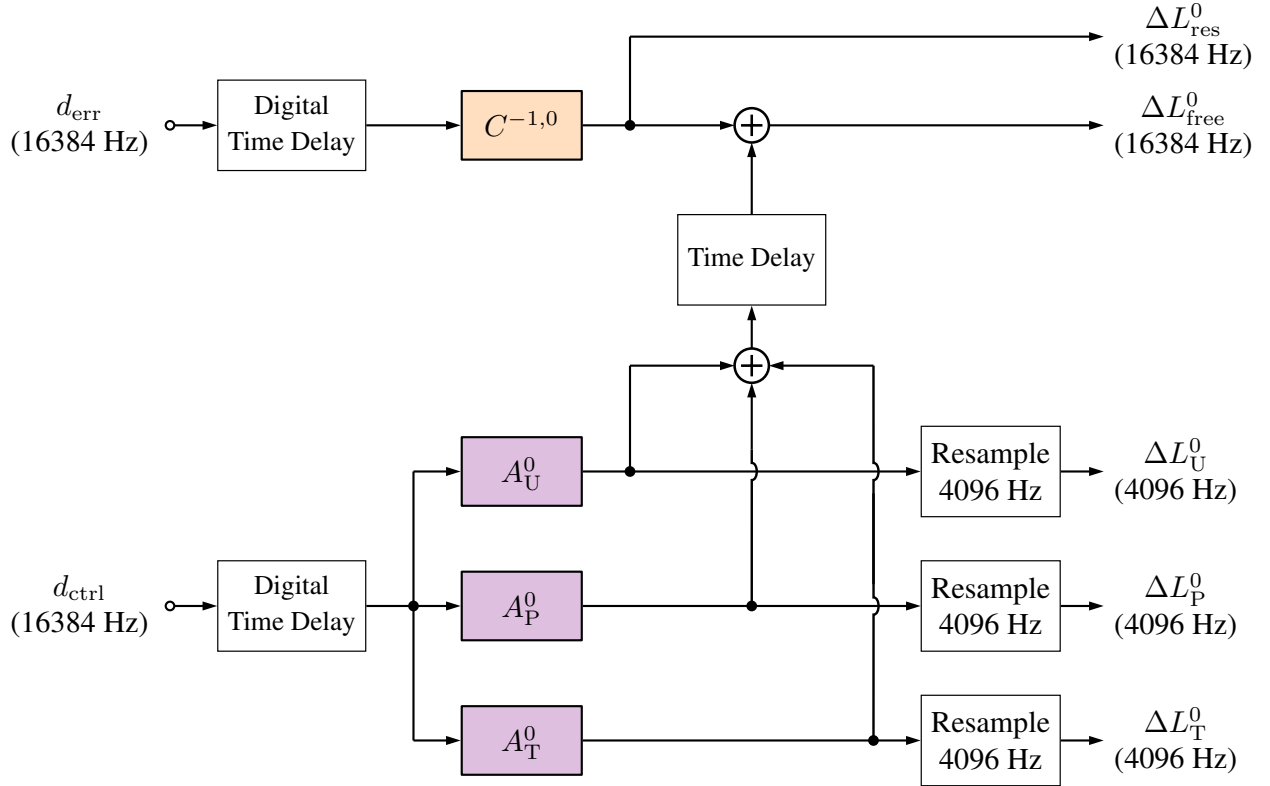


FIG. 5. Simplified diagram of the front-end calibration pipeline. The digital error  $d_{\text{err}}$  and digital control  $d_{\text{ctrl}}$  signals are picked off from the DARM model in the front-end computers. This process adds a single digital-sampling-period delay in the  $d_{\text{err}}$  and  $d_{\text{ctrl}}$  signals, shown above as the “Digital Time Delay” box. The error and control signals are then filtered with the relevant IIR filter representations for the inverse sensing function and the actuation function, respectively. The control signal chain is delayed by an amount representing the net delay between the control and error signal chains before being combined with the error signal to form  $\Delta L_{\text{free}}^0$ . The filtered control and error signals are also outputted from the pipeline. Details of the calculation of the time-dependent correction factors (TDCFs) are not shown.

*Pick off error and control signals* Since the error and control digital signals  $d_{\text{err}}$  and  $d_{\text{ctrl}}$  are picked off from the DARM front-end model and passed to the front-end calibration model, there is a one digital-sampling-period delay, which, at a sample rate of 16384 Hz, is equivalent to a  $61 \mu\text{s}$  delay.

*Apply IIR filters* The IIR filters for the inverse sensing function are applied to the  $d_{\text{err}}$  signal to produce  $\Delta L_{\text{res}}^0$ , which is also written out as a partially calibrated output at a sample rate of 16384 Hz. The  $d_{\text{ctrl}}$  signal is split into three equivalent chains. One chain is filtered with the IIR filter models for the upper intermediate actuation function  $A_U^0$ , another one is filtered with the IIR filter models for the penultimate actuation function  $A_P^0$ , and the third one is filtered with the IIR filter models for the test actuation function  $A_T^0$ .

*Resample  $\Delta L_{\text{P,U,T}}^0$  outputs* After  $d_{\text{ctrl}}$  is filtered with the three stages of the actuation, the output of each of these filtering processes is resampled from 16384 Hz down to 4096 Hz and written out as the partially calibrated front-end control outputs  $\Delta L_{\text{P}}^0$ ,  $\Delta L_{\text{U}}^0$ , and  $\Delta L_{\text{T}}^0$ . This downsampling is done to reduce the amount of storage memory required to save these data.

*Combine and apply delay for  $\Delta L_{\text{ctrl}}^0$*  The filtered output of the actuation chain (before it is resampled down to 4096 Hz) is combined together to form  $\Delta L_{\text{ctrl}}^0$  at a sample rate of 16384 Hz. A delay is then applied to  $\Delta L_{\text{ctrl}}^0$ . The delay that is applied is the relative delay between the control and the residual chains to ensure they combine with the correct phase. This delay requires sub-sample phase accuracy and is implemented using a Thiran fractional delay filter [37].

*Compute  $\Delta L_{\text{free}}^0$*  The partially calibrated residual output  $\Delta L_{\text{res}}^0$  and the partially calibrated, combined control output  $\Delta L_{\text{ctrl}}^0$  are added together to form  $\Delta L_{\text{free}}^0$  at sample rate of 16384 Hz. This is the fully calibrated output of the front-end calibration pipeline.

### 3. Time-dependent correction factors

The reference sensing and actuation functions used in the front-end model are mostly static, i.e., they are obtained from a set of measurements done at the beginning of each observing run. However, as mentioned in Sec. II C, the sensing and

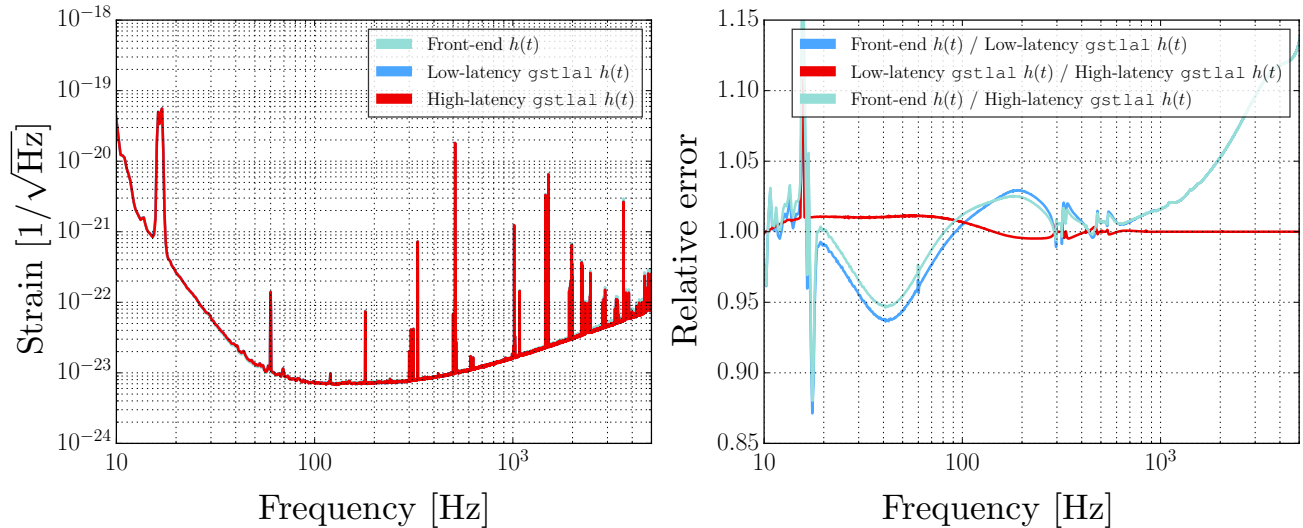


FIG. 6. A comparison of the output from the front-end calibration pipeline, low-latency `gstlal` calibration pipeline, and high-latency `gstlal` calibration pipeline. The plot on the left shows the amplitude spectral density (ASD) for each of the pipelines at L1 during the second observing run. The right plot shows the ratio of the ASDs of the front-end  $h(t)$  to the low-latency `gstlal`  $h(t)$  and the ratio of the ASDs of the low-latency `gstlal`  $h(t)$  to the high-latency `gstlal`  $h(t)$ . The calibration undergoes about a 5-10% improvement between the front-end  $h(t)$  and the low-latency `gstlal`  $h(t)$  and an additional few percent improvement between the low-latency `gstlal`  $h(t)$  and the high-latency `gstlal`  $h(t)$ . The biggest cause for the improvement from the front-end  $h(t)$  to the low-latency `gstlal`  $h(t)$  is the application of some of the TDCFs in the low-latency `gstlal`  $h(t)$ .

actuation functions are not static but change over time due to changes in the physical configurations of interferometric control loops. The infrastructure to track the TDCFs is built into the front-end calibration model.

The TDCFs are computed as outlined in Sec. II C, Appendix A, and Ref. [14]. Some details of the implementation of these calculations in the front-end calibration pipeline are discussed here. In order to compute the TDCFs, several data streams need to be demodulated at given calibration line frequencies. The demodulation technique used by the front-end calibration pipeline is to first mix a local oscillator at the given frequency with the incoming signal, then apply a low-pass filter with a corner frequency of 0.1 Hz to the mixed output, and finally perform a 128 second running average on the demodulated result. The running average is performed by using a low-pass filter with a corner frequency of  $\approx 0.008$  Hz. Once each of the relevant signals is demodulated at the necessary calibration line frequencies, the remaining calculation of the TDCFs follows from Eqs. (A7), (A9), (A11), and (A12).

The TDCFs are not used to constantly correct the sensing and actuation functions in the front-end calibration pipeline. This is mainly due to the long response time of the IIR filters used in the front-end models that suffer from lasting effects of small transients. For this reason and for reasons mentioned below, an additional low-latency pipeline, the `gstlal` calibration pipeline, is used to produce more accurately calibrated  $h(t)$  data.

#### 4. Benefits and limitations of front-end calibration pipeline

A clear benefit of the front-end calibration process is that calibrated strain data can be produced in real time. Since the future of gravitational-wave astronomy relies on very low-latency detection candidate identification, we are working on moving the entire calibration process into the front-end pipeline in the future. However, this work is still in its initial stage.

The current level of accuracy of  $\Delta L_{\text{free}}^0$  is relatively poor when compared to the other calibrated data products discussed in the next sections. Systematic errors are introduced by the IIR filters, and it is challenging to build IIR filters that accurately model super-Nyquist features of the calibration. We have, however, had good success in modeling these features using FIR filters, which will be discussed more below. Finally, as mentioned above, the front-end calibration pipeline currently cannot apply the TDCFs to correct the sensing and actuation functions also due to limitations involved with using IIR filtering. Altogether, this results in the front-end calibration having systematic errors on the level of a few percent in the mid-frequency region (50-500 Hz) and up to 10% between 1 kHz - 3 kHz. Additionally, we can't apply a phase advance in the real-time code used by the front-end calibration pipeline, and this results in initially recorded data with a fixed and known number of cycles of delay, relative to their actual occurrence in the interferometer.

The limitations of the front-end calibration pipeline are circumvented by picking off the outputs  $\Delta L_{\text{res}}^0$ ,  $\Delta L_{\text{U}}^0$ ,  $\Delta L_{\text{P}}^0$  and  $\Delta L_{\text{T}}^0$  and applying corrections to these outputs before combining them to form  $h(t)$ . The next section will discuss the low-latency

`gstlal` calibration pipeline that performs this procedure.

### B. The Low-Latency `gstlal` Calibration Pipeline

The low-latency `gstlal` calibration pipeline takes in the partially calibrated data outputted by the front-end calibration pipeline and applies additional filters to correct for uncompensated components and time delays, as discussed in Sec. III A. The inputs to this pipeline are the partially calibrated data rather than the original  $d_{\text{err}}$  and  $d_{\text{ctrl}}$  signals in order to take advantage of the realtime nature of parts of the front-end calibration model. For example, when suspension or actuation filters are changed in the DARM model, the front-end calibration model will have immediate access to these filters. By using the partially calibrated data from the front-end calibration pipeline, the low-latency `gstlal` calibration pipeline will be using accurate to realtime calibration models.

The `gstlal` calibration pipeline is also used for all high-latency recalibration that may be required, as is discussed more in Sec. III C. Both the low- and high-latency `gstlal` calibration pipelines use finite impulse response (FIR) filters. The reasons for using FIR filters instead of IIR filters, which are used by the front-end calibration pipeline, are the following: 1) When recalibrating the data offline, it is useful to recalibrate the data in short, parallelized stretches, which requires FIR filters as opposed to IIR filters; 2) The low-latency calibration system uses both a primary calibration pipeline setup and a redundant pipeline setup to safeguard against online system failures, and in order for the output of the primary and redundant pipelines to be identical, the pipelines cannot depend on their start time or long-term history; 3) All calibration products outside of the front-end need to be reproducible for arbitrarily chosen start times and durations. An example release version of the `gstlal` calibration pipeline can be found in [38].

The low-latency `gstlal` calibration pipeline produces a more accurate  $h(t)$  than the front-end calibration pipeline. The additional corrections applied by the `gstlal` calibration pipeline modify the frequency response as illustrated in Fig. 6.

#### 1. FIR filters

We use FIR filters to model the super-Nyquist features of the calibration that are not captured by the front-end calibration pipeline, corrections for systematic errors introduced by the IIR filters used in the front-end calibration pipeline, and accurate time delays in both the sensing and actuation functions. The process for creating discrete representations, FIR filters, from established continuous representation models of the sensing and actuation is the following:

1. *High-pass filter* Seismic noise in the raw data channels is too high at low frequencies to measure any GW signals, and the digital system has finite dynamic range. Low frequencies are therefore rolled off by multiplying the frequency components below 9 Hz by half of a Hann window raised to the fourth power.

2. *For sensing chain only: Low-pass filter* Since the inverse sensing function tends toward infinity at high frequencies, a low-pass filter is applied to the inverse sensing function to roll off high frequencies ( $f \gtrsim 6$  kHz) smoothly. This is done by multiplying the high frequency components by half of a Hann window.
3. *Artificial delay* An artificial delay is added to the FIR filter that is set to be half of the length of the filter. This delay is undone within the `gstlal` calibration pipeline by advancing the filter output by an equivalent number of samples. The reason for the delay is to center the FIR filter in time.
4. *Inverse Fourier transform* The Nyquist component is zeroed out and then we take the inverse Fourier transform to compute the FIR time-domain filter.
5. *Tukey window* A Tukey window is applied to the resulting time-domain FIR filter to ensure it falls off smoothly at the beginning and end of the time-domain filter response. All of the above steps are performed using standard Matlab software packages [39].

The fidelity of the FIR filters is checked by taking the Fourier transform of the final FIR filter with the artificial delay removed and comparing the resulting magnitude and phase to the original frequency-domain model. Example comparison plots are shown in Fig. 7. The differences between the frequency response of the FIR filter and the original frequency domain model are less than 0.01 % in magnitude and 0.01° in phase from 10 Hz to 8 kHz.

#### 2. Low-latency `gstlal` calibration pipeline overview

Here, we outline the methods used in low latency by the `gstlal` calibration pipeline to process the partially calibrated data read in from the front-end calibration pipeline and produce the final calibration product,  $h(t)$ . Fig. 8 shows a simplified diagram of the pipeline.

Rather than reading in the final calibration product of the front-end,  $\Delta L_{\text{free}}^0$ , the `gstlal` calibration pipeline reads in the components of  $\Delta L_{\text{free}}^0$  separately. The contribution from the actuation is split into three parts, corresponding to the lowest three stages of the actuation:  $\Delta L_{\text{T}}^0$ ,  $\Delta L_{\text{P}}^0$ , and  $\Delta L_{\text{U}}^0$ . The contribution from the inverse sensing function is  $\Delta L_{\text{res}}^0$ . The following procedure describes the workflow of the low-latency `gstlal` calibration pipeline chronologically:

*Fill in missing data* Sometimes, chunks of data in one or more channels being read in by the `gstlal` calibration pipeline are missing or corrupted. These dropouts generally occur with a frequency of a few per week and can range from one second in length to several hours in some cases. Oftentimes, they occur in all the input channels at once, but this is not always the case. This missing or corrupted data is filled in at the beginning of the pipeline and timestamped appropriately to produce a continuous stream. Most channels are filled in with zeros, except for the coherence uncertainty channels (discussed in Appendix B),

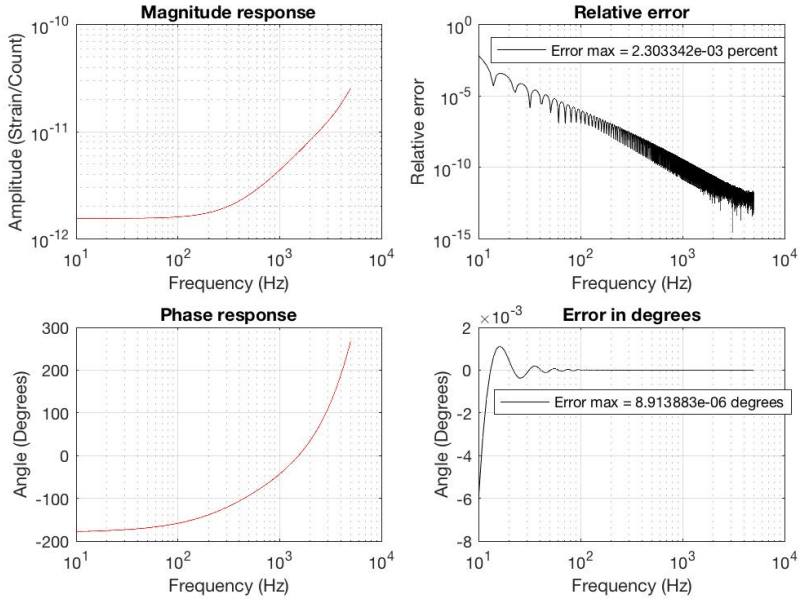


FIG. 7. Comparison of the inverse sensing FIR filter to the inverse sensing model. The left panel shows a bode plot of the frequency response of an example inverse sensing FIR filter for L1 (red) and the original inverse sensing model (blue). The top right plot shows the relative error in magnitude between the original model and the frequency response of the FIR filter. The bottom right plot shows the phase difference in degrees between the original model and the frequency response of the FIR filter. As can be seen in the plots, the FIR filter is a very accurate representation of the derived model for the inverse sensing function above 10 Hz.

which are filled in with ones. This replacement also occurs when an input sample's magnitude is outside of the expected range of  $[10^{-35}, 10^{35}]$ , to prevent arithmetic underflows and overflows.

Add  $\Delta L_p^0$  and  $\Delta L_u^0$  Since the same FIR filter and time-dependent correction are applied to both,  $\Delta L_p^0$  and  $\Delta L_u^0$  can be added before filtering, to save computational cost. The result is referred to as  $\Delta L_{pu}$ .  $\Delta L_T^0$  is not combined because it receives a separate time-dependent correction factor  $\kappa_T(t)$ .

*Downsample the actuation channels* The three actuation channels are read into the `gstlal` calibration pipeline at a sample rate of 4096 Hz. To keep computational costs manageable, this is downsampled to 2048 Hz before applying the FIR correction filters. This is necessary for only the actuation channels, due to the longer filter length (discussed more below). The downsampling is done using the stock GStreamer element `audioreresample` [40]. A sinc table is used to filter the input before downsampling, in order to minimize aliasing effects.

*Apply FIR filters* The FIR correction filters, made through the process described in Section III B 1, are applied to correct the front-end estimates of the components of DARM:

$$\Delta L_T^1(t) = [A_{\text{corr}} * \Delta L_T^0](t), \quad (12a)$$

$$\Delta L_{pu}^1(t) = [A_{\text{corr}} * \Delta L_{pu}^0](t), \quad (12b)$$

$$\Delta L_{\text{res}}^1(t) = [C_{\text{corr}}^{-1} * \Delta L_{\text{res}}^0](t), \quad (12c)$$

where  $C_{\text{corr}}^{-1}$  is the digital filter applied to correct the front-end estimate of the residual displacement, and  $A_{\text{corr}}$  corrects the front-end estimate of the controlled length differential. This

correction is the same for all three stages of the actuation because the components that cannot be modelled in the front end, such as time delays and anti-imaging filters, are the same for each stage. As a reminder, superscript 0's and 1's are used to denote quantities associated with the front-end and the low-latency `gstlal` calibration pipeline, respectively.

Since the inverse sensing chain contains most of the information above 1 kHz (see Fig. 9), it is necessary to filter it at the full  $h(t)$  sample rate of 16384 Hz. The inverse sensing correction filter  $C_{\text{corr}}^{-1}$  is 1 second in length and accounts for roughly half of the computational cost of running the pipeline. The actuation filters are 6 s in length, mainly because the actuation channels output from the front end have a lot of noise below 10 Hz, which requires a longer filter to attenuate sufficiently. Due to the length of these filters, it is necessary to filter at 2048 Hz instead of the original actuation sample rate of 4096 Hz outputted by the front end. Since the actuation chain contributes very little to the total strain above 1 kHz (see Fig. 9), this has minimal impact on the integrity of the calibration.

The FIR filtering is performed in the time domain through direct convolution. The timestamps of the filtered result are then advanced the appropriate amount to compensate for the artificial delay that was built into the FIR filters. To test timestamp accuracy, the calibration lines injected with the photon calibrator can be recovered from  $h(t)$  and compared in phase with the injected sinusoids. This was done with three of the calibration lines at L1, and the measured timestamp differences were negligibly small compared to the sampling periods of the filters.

The artificial delay built into the FIR filters is half the length

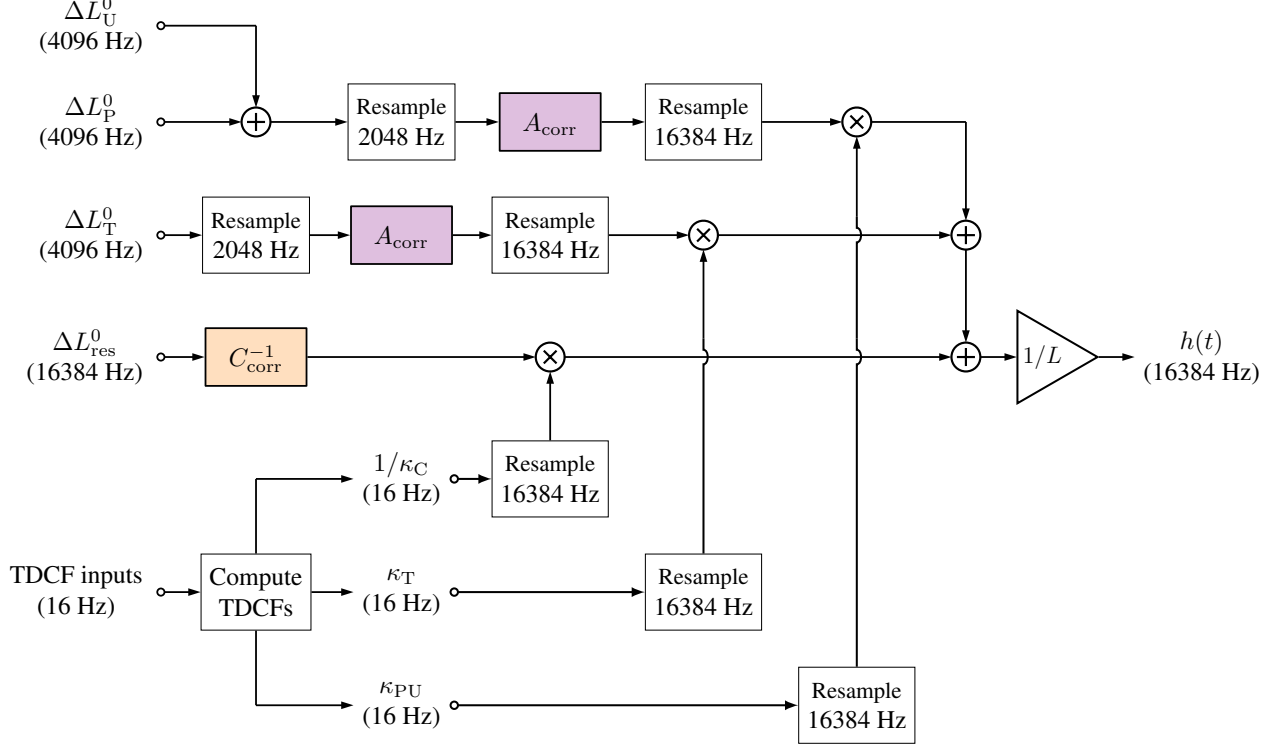


FIG. 8. Simplified diagram of the low-latency `gst1al` calibration pipeline. The partially-calibrated outputs of the front-end calibration pipeline are ingested and then filtered by the appropriate FIR filters for the actuation and inverse sensing chains. The filtered output is corrected by the TDCFs and added together. The result is divided by  $L$  to give the final results for  $h(t)$ . The residual correction filter  $C_{\text{corr}}^{-1}$  is 1 second in length, and the actuation correction filter  $A_{\text{corr}}$  is 6 seconds in length. Details of the calculation of the time-dependent correction factors (TDCFs) and the state vector calculation are not shown.

of the FIR filter. Therefore, filtering of the actuation chain adds a latency of 3 seconds to the output of the pipeline, due to the 6-second length of the actuation filters. This is a significant fraction of the 5 - 9 s latency of the low-latency `gst1al` calibration pipeline. Much of the remaining latency is due to the 4-second length of output  $h(t)$  data files, which also accounts for the stated range in latency.

*Upsample the actuation channels* After filtering at 2048 Hz,  $\Delta L_T^1(t)$  and  $\Delta L_{\text{PU}}^1(t)$  are upsampled to the full  $h(t)$  sample rate of 16384 Hz. A sinc table is again used to filter the input, to attenuate frequencies close to the Nyquist frequency of 8192 Hz.

*Apply time-dependent correction factors* The time-dependent correction factors (TDCFs), discussed in Section III B 3 and in more detail in [14], are applied at 16384 Hz after applying the correction FIR filters. The residual displacement  $\Delta L_{\text{res}}^1(t)$  is divided by  $\kappa_C(t)$  in a sample-by-sample manner to correct for the time-dependence of the optical gain. The test stage component of the controlled displacement  $\Delta L_T^1(t)$  is multiplied by  $\kappa_T(t)$  to correct for the time-dependence of the ESD actuation strength. Currently, the time-dependence of the penultimate and upper intermediate stages of the actuation is accounted for by a single value,  $\kappa_{\text{PU}}(t)$ , which multiplies

$\Delta L_{\text{PU}}(t)$ <sup>2</sup>. Correcting the filtered output with the TDCFs as a simple multiplication in the time domain is possible because their variation in time is slow compared to the lowest frequencies in the calibrated frequency band.

*Add inverse sensing and actuation chains* With correction FIR filters and time-dependent corrections applied, the residual displacement is added with the sum of the two controlled displacements to produce the measured free disturbance,  $\Delta L_{\text{free}}^1$ . This is divided by the average IFO arm length  $L$  to produce the strain  $h(t)$ .

### 3. Time-dependent correction factors

Because it is not possible to take broadband calibration measurements while observing, we continuously inject sinusoidal

<sup>2</sup> We note here that computational cost could be reduced if the TDCFs were applied and the actuation channels summed before filtering, since the control correction filter would only be applied once. However, due to the excess noise below 10 Hz in the front-end output, multiplying by the TDCFs before high-pass filtering adds significant noise in the relevant frequency band due to noisy fluctuations in the TDCFs.

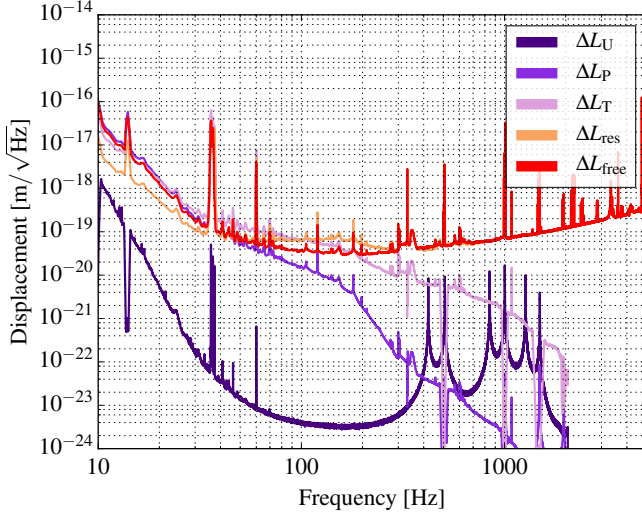


FIG. 9. Amplitude spectral densities for  $\Delta L_{\text{res}}$ ,  $\Delta L_{\text{T}}$ ,  $\Delta L_{\text{P}}$ ,  $\Delta L_{\text{U}}$ , and  $\Delta L_{\text{free}}$  across the relevant frequency band at H1. These were obtained as intermediate products from the `gstlal` calibration pipeline. Note the visible calibration lines:  $f_{\text{T}} = 35.9$  Hz, injected with the ESD, and  $f_{\text{pc}} = 36.7$  Hz,  $f_2^{\text{pc}} = 331.9$  Hz, and  $f_3^{\text{pc}} = 1083.7$  Hz, injected with the photon calibrator.

excitations at select frequencies into the IFOs using the photon calibrator and the actuation system, and then measure the amplitude and phase of these calibration lines in the error signal  $d_{\text{err}}$ , as described in Sec. II C. In order to measure changes in the actuation and sensing functions of the IFO using the excitations and the error signal, we need an algorithm to extract the relative amplitude and phase of each of the relevant calibration lines in both the injection channel and the error signal. To demodulate a time series, we first multiply each sample by  $e^{-i\omega t}$ , where  $t$  is the GPS time associated with that sample and  $\omega$  is the angular frequency of a calibration line. We then downsample to 16 Hz to keep computational cost manageable and apply a low-pass filter  $H$ . The result is a complex value representing the amplitude and phase of the calibration line of interest in the signal being measured. For an oscillation with amplitude  $a$  and phase angle  $\phi$ ,

$$H * \{e^{-i\omega t} [a \cos(\omega t - \phi) + n(t)]\} = \quad (13)$$

$$H * \left\{ \frac{a}{2} [e^{-i\phi} + e^{i(-2\omega t + \phi)}] + n(t)e^{-i\omega t} \right\} \approx \frac{a}{2} e^{-i\phi},$$

where  $n(t)$  is noise, that is, anything other than the sinusoidal injection.

The downsampling to 16 Hz is necessary to prevent unmanageable computational cost associated with low-pass filtering and computing the TDCFs. However, downsampling a time series containing a  $\sim 300$  Hz oscillation to 16 Hz would cause aliasing. Therefore, an anti-aliasing filter is included in the resampling process.<sup>3</sup> This effectively forms part of the low-pass

<sup>3</sup> Due to the need to process complex data, the element used here is different from the one used for resampling the actuation chain.

filtering process. The low-pass filter applied after downsampling is a 20 second Hann window applied in the time domain at 16 Hz. After this, the TDCFs are computed as described in Sec. II C and Appendix A.

Although the calculation of the TDCFs is running constantly, it produces an accurate result only when the IFO is in a low-noise state, and even then, the resulting time series is quite noisy. We describe the procedure used to manage this issue in Appendix B.

$\kappa_{\text{T}}$ ,  $\kappa_{\text{PU}}$ , and  $\kappa_{\text{C}}$  are used to correct  $h(t)$  as described in Sec. III B 2, while the time-dependence of the coupled cavity pole  $f_{\text{cc}}$  is not corrected for, as such a frequency- and time-dependent correction would require the ability to update FIR filters while the calibration pipeline is running. This is a current area of development and is expected to be implemented in the `gstlal` calibration pipeline before LIGO's third observing run. This feature would also allow compensation for effects caused by the detuning of the SRC. The optical spring frequency and quality factor of the SRC are currently being tracked at H1, but their time-dependence is not compensated for in  $h(t)$ . The calculation of these parameters is outlined in Appendix A.

#### 4. State vector

In addition to computing  $h(t)$ , the `gstlal` calibration pipeline also computes a bitwise state vector that denotes the integrity of  $h(t)$  at a sample rate of 16 Hz. The top level bits of the state vector are the summary bits used to determine whether or not  $h(t)$  should be used for astrophysical analysis. For more details about the state vector definition during the second observing run, see Appendix C.

### C. High-latency `gstlal` Calibration Pipeline

The `gstlal` calibration pipeline is also used to produce a second calibration of the archived raw data in high latency. As stated above, the most common reasons for recalibrating the data are dropouts of data somewhere in the low-latency system and improved models for the calibration developed over time. For example, during Advanced LIGO's first observing run, the TDCFs were used to correct  $h(t)$  only in the high-latency calibration. The `gstlal` calibration pipeline run in high latency is quite similar to its low-latency counterpart and is depicted in Fig. 10.

Instead of reading in the partially-calibrated outputs of the front-end, we calibrate in high latency using  $d_{\text{err}}$  and  $d_{\text{ctrl}}$  directly.<sup>4</sup> Therefore, the FIR filters applied by the high-latency pipeline contain the full static reference models for the inverse

<sup>4</sup> While it would certainly be possible to approach the high-latency calibration with the same methodology as the low-latency calibration, which is to correct the output of the front-end calibration pipeline, it is often impractical to develop the appropriate correction filters that model all the changes occurring in the front-end calibration pipeline during an observing run due to changes caused by human error that inevitably occur in realtime systems.

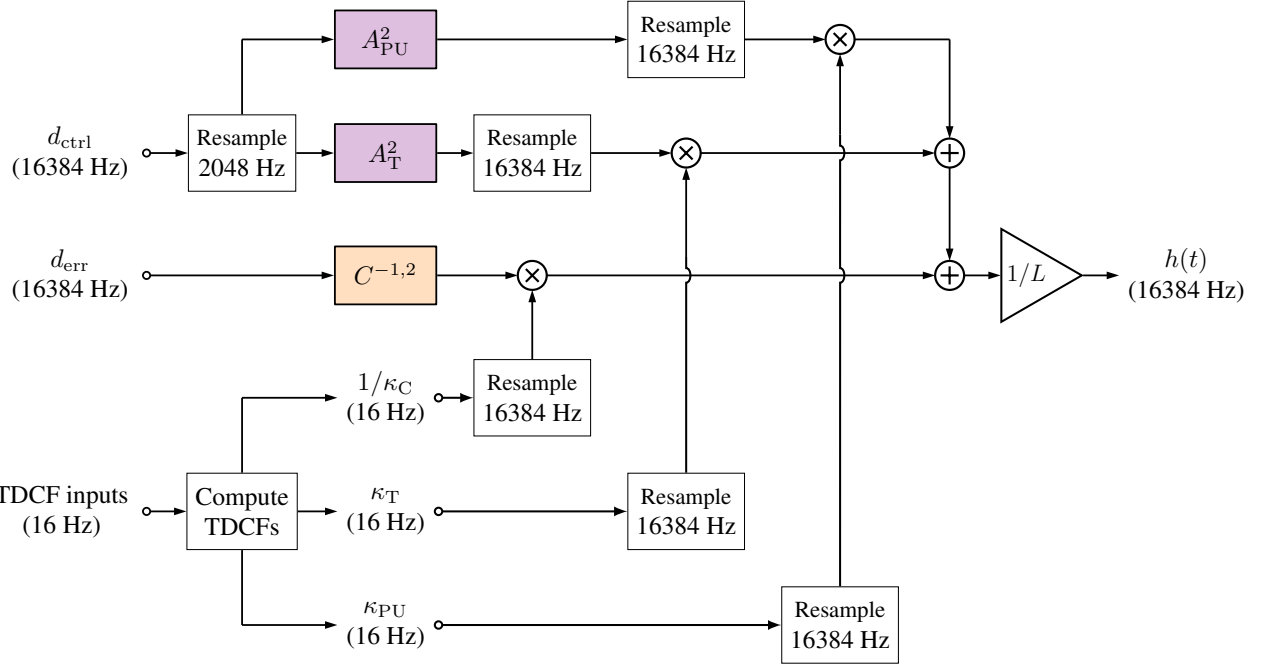


FIG. 10. Diagram of the high-latency `gstl1` calibration pipeline. The digital error  $d_{\text{err}}$  and digital control  $d_{\text{ctrl}}$  signals are calibrated directly using the full inverse sensing and actuation models. Just as with the low-latency `gstl1` calibration pipeline, the error and control chains are corrected with the appropriate TDCFs. A superscript 2 indicates association with the high-latency `gstl1` calibration pipeline. Details of the TDCFs calculation and the state vector calculation are not shown.

sensing and the actuation. Otherwise, the production of the filters is equivalent to the the description given in Section III B 1. In the high-latency calibration, the model-based constants used in computing the TDCFs are recorded in a file which is ingested into the `gstl1` calibration pipeline. This is in contrast to these constants being read in as recorded directly from the front-end systems. This allows us to correct large systematic errors in the TDCFs caused by mistakes made in low-latency in recording these factors in the front-end system.

The high-latency calibration is generally produced weeks to months after acquisition of raw data products, such as  $d_{\text{err}}$  and  $d_{\text{ctrl}}$ . The production of high-latency calibration is accomplished through many jobs run in parallel on the LIGO Data Grid computing clusters [41]. Each job involves producing 4096 seconds of calibrated data, using the corresponding stretch of  $d_{\text{err}}$  and  $d_{\text{ctrl}}$  with the addition of several minutes of input data at the beginning and end, to allow all filtering processes to settle.

In general, differences between the low-latency and high-latency versions of calibration can vary widely, depending on whether significant systematic errors exist in low-latency that can be corrected in high-latency. For the majority of the second observing run, however, differences are under 2 % in magnitude from 10 Hz to 8 kHz. Fig. 6 includes a comparison of the amplitude spectral density for  $h(t)$  at L1 as computed by both the low-latency `gstl1` calibration pipeline and the high-latency `gstl1` calibration pipeline.

#### IV. CONCLUSION

During advanced LIGO’s first two observing runs, the low-latency GW strain  $h(t)$  was produced in the time domain using a combination of IIR filtering processes in the front-end computers and FIR filtering processes in the downstream `gstl1` calibration pipeline. The `gstl1` calibration pipeline also applies time-dependent correction factors to the actuation and sensing components of  $h(t)$  to improve calibration accuracy in the relevant frequency band. The `gstl1` calibration pipeline is used in high latency to produce an additional, more accurate calibration that corrects for missing data and some known systematic errors in the low-latency  $h(t)$  data. During O2, the systematic error and uncertainty achieved by the high-latency calibration (as well as much of the online calibration) is less than 5 % in magnitude and 3° in phase in the relevant frequency band of 20 Hz to 1 kHz. For details of the frequency-dependent uncertainty budget for O2, see [13].

In the future, we hope to improve the latency and accuracy of the low-latency calibration data products. Work is in progress to implement a method for applying time- and frequency-dependent corrections, i.e., for the time-dependence of the cavity pole  $f_{\text{cc}}$  and the optical spring frequency  $f_s$  and quality factor  $Q$  of the SRC. As described in Sec. II C and Appendix A, these are already computed in both the front-end and the `gstl1` calibration pipeline. In order to compensate for their time-dependence and improve  $h(t)$  accuracy, an algorithm

to compute a new inverse sensing filter and smoothly replace the previous filter is being developed. The time-dependence of the cavity pole is known to be a significant contributor to systematic error in  $h(t)$  across the relevant frequency band (see, e.g., Fig. 4). The time-dependence of  $f_s$  and  $Q$  is significant at H1 in the lowest frequency band of concern, mainly below about 20 Hz. An additional change that should lead to a small improvement in the calibration is to compute  $\kappa_p$  and  $\kappa_u$  individually instead of tracking and applying their approximate combined effect in the `gst1a1` calibration pipeline as  $\kappa_{pu}$ . This would better represent the true model of the actuation as expressed in Eq. (11), and it could have an impact at low frequencies as  $\Delta L_p$  and  $\Delta L_u$  differ in their frequency dependence (see Fig. 9).

The online calibration latency has improved during O2 by about 5 seconds. This was mainly due to the removal of the latency associated with applying an anti-aliasing filter during the resampling required for the calculation and application of the TDCFs. Further improvements can be made, primarily in two ways: 1) The length of the GW frame files could be reduced from four seconds to one second; 2) The length of the actuation filter in the `gst1a1` calibration pipeline can be reduced. Shortening the actuation filters is straightforward, but if not done with care, spectral leakage will corrupt the  $h(t)$  spectrum. For this reason, we plan to incorporate more effective high-pass filtering into the FIR filters, as the current methodology involves simply rolling off low frequencies with half of a Hann window raised to the fourth power (first step in Section III B 1).

Work is also underway to develop a complete front-end calibration model, as the eventual goal of the LIGO calibration team is to perform the low-latency calibration entirely in the front-end computers. The primary challenges that must be overcome to realize a complete front-end calibration are the ability to implement FIR filtering and to assign timestamps to data that are not real time. There are several advantages to having the low-latency calibration entirely in the front end. The front end's direct access to IFO models and parameters may reduce the occurrence of human errors in calibration. Calibrating in the front end also removes data transfer steps, reducing the likelihood of data dropouts.

Overall, the calibration process for Advanced LIGO has been expanded to include a very low-latency calibrated strain data product and an unprecedented level of accuracy in the final, high-latency strain data when compared with Initial LIGO. Typical calibration uncertainty levels in Initial LIGO ranged from 10 % in magnitude and 10° in phase to 20 % in magnitude and 20° in phase [42], while results for the calibration uncertainty around the time of GW170104 [4] are less than 5 % in magnitude and 3° in phase [13]. Future Advanced LIGO observing runs promise further improvement to both the latency and accuracy of the calibration process with an end-goal of having real-time calibrated strain data with percent-level accuracy available for analysis. Such an achievement will help push the envelope forward for the new era of gravitational-wave astronomy and multi-messenger astronomy.

## ACKNOWLEDGMENTS

The authors would like to thank Chris Wipf, Evan Hall, Jolien Crieghton, Patrick Brockill, John Zweizig, Kipp Cannon, Bruce Allen, Chris Pankow, Chad Hanna, and Les Wade for helpful discussions and feedback while developing the methods discussed here. The authors were supported by National Science Foundation grants PHY-1607178, PHY-1607585, and PHY-1506360. LIGO was constructed by the California Institute of Technology and Massachusetts Institute of Technology with funding from the National Science Foundation and operates under cooperative agreement PHY-0757058. This paper carries LIGO Document Number LIGO-P1700236.

## Appendix A: Calculation of Time-dependent Correction Factors

As discussed in Sec. II C, the time-dependent correction factors (TDCFs) in the calibration are measured using known sinusoidal injections (i.e. *calibration lines*). The factor  $\kappa_T$  is measured using the  $f_T$  and  $f_1^{\text{pc}}$  lines, while  $\kappa_{\text{PU}}$  is measured using the  $f_{\text{ctrl}}$  and  $f_1^{\text{pc}}$  lines. All three of these lines are placed over a small band between 10 and 40 Hz, where the stages of the actuation function are comparable in magnitude, to reduce systematic errors. The quantities  $\kappa_C$  and  $f_{\text{cc}}$  are measured using the  $f_2^{\text{pc}}$  line, which is placed near 330 Hz in the middle of Advanced LIGO's most sensitive frequency band. The quantities  $f_s$  and  $Q$  are measured by the lowest Pcal line  $f_4^{\text{pc}}$ , placed near 8 Hz where their effect is significant. The remaining line  $f_3^{\text{pc}}$  is used as a sanity check on calibration uncertainty above 1 kHz. Table II summarizes the purpose of each calibration line.

TABLE II. Summary of the purpose of each calibration line.

Line	Purpose	Frequency
$f_{\text{ctrl}}$	Computation of $\kappa_{\text{PU}}$	10 - 40 Hz
$f_T$	Computation of $\kappa_T$	10 - 40 Hz
$f_1^{\text{pc}}$	Computation of $\kappa_T$ and $\kappa_{\text{PU}}$	10 - 40 Hz
$f_2^{\text{pc}}$	Computation of $\kappa_C$ and $f_{\text{cc}}$	$\sim 330$ Hz
$f_3^{\text{pc}}$	Check on high-frequency calibration	$\sim 1$ kHz
$f_4^{\text{pc}}$	Computation of $f_s$ and $Q$	$\sim 8$ Hz

To solve for the time-dependent correction factors (TDCFs), we need to know their effect on the amplitude and phase of the calibration lines in  $d_{\text{err}}$ . From Fig. 2,

$$\tilde{d}_{\text{err}} = \kappa_C \frac{\tilde{C}_{\text{res}}}{1 + i f / f_{\text{cc}}} (\tilde{\Delta L}_{\text{free}} + \tilde{x}_{\text{pc}} - \tilde{\Delta L}_{\text{ctrl}}), \quad (\text{A1})$$

where  $\tilde{C}_{\text{res}}$  is the static reference model sensing function with dependence on the cavity pole removed. Note that we have neglected the detuning of the signal recycling cavity, as this has little impact at the calibration line frequencies used to compute  $\kappa_T$ ,  $\kappa_{\text{PU}}$ ,  $\kappa_C$ , and  $f_{\text{cc}}$ . Referring to Fig. 2, we see that

$$\tilde{\Delta L}_{\text{ctrl}} = \kappa_T \tilde{A}_T (\tilde{D} \tilde{d}_{\text{err}} + \tilde{x}_{\text{ctrl}} - \tilde{x}_T) + \kappa_{\text{PU}} \tilde{A}_{\text{PU}} (\tilde{D} \tilde{d}_{\text{err}} + \tilde{x}_{\text{ctrl}}). \quad (\text{A2})$$

Solving for  $\tilde{d}_{\text{err}}$  in terms of the injected excitations, we obtain the expression

$$\tilde{d}_{\text{err}} = \frac{\tilde{\Delta L}_{\text{free}} + \tilde{x}_{\text{pc}} - \kappa_T \tilde{A}_T (\tilde{x}_{\text{ctrl}} - \tilde{x}_T) - \kappa_{\text{PU}} \tilde{A}_{\text{PU}} \tilde{x}_{\text{ctrl}}}{(S \tilde{C}_{\text{res}})^{-1} + (\kappa_T \tilde{A}_T + \kappa_{\text{PU}} \tilde{A}_{\text{PU}}) \tilde{D}}, \quad (\text{A3})$$

where we have defined

$$S \equiv \frac{\kappa_C}{1 + i f / f_{\text{cc}}}. \quad (\text{A4})$$

To solve for  $\kappa_T$ , we demodulate  $d_{\text{err}}$  at the ESD calibration line  $f_T$  and the first photon calibrator line  $f_1^{\text{pc}}$ , which are separated

by only  $\sim 1$  Hz. This yields two simple equations:

$$\tilde{d}_{\text{err}}(f_T) = \frac{\kappa_T \tilde{A}_T \tilde{x}_T}{(S \tilde{C}_{\text{res}})^{-1} + (\kappa_T \tilde{A}_T + \kappa_{\text{PU}} \tilde{A}_{\text{PU}}) \tilde{D}} \Big|_{f_T} \quad (\text{A5})$$

and

$$\tilde{d}_{\text{err}}(f_1^{\text{pc}}) = \frac{\tilde{x}_{\text{pc}}}{(S \tilde{C}_{\text{res}})^{-1} + (\kappa_T \tilde{A}_T + \kappa_{\text{PU}} \tilde{A}_{\text{PU}}) \tilde{D}} \Big|_{f_1^{\text{pc}}}. \quad (\text{A6})$$

Then, we take the following ratios of  $\tilde{d}_{\text{err}}$ ,  $\tilde{x}_{\text{pc}}$ , and  $\tilde{x}_T$  at the two line frequencies to estimate  $\kappa_T$ :

$$\kappa_T \approx \frac{1}{\tilde{A}_T(f_T)} \cdot \frac{\tilde{d}_{\text{err}}(f_T)}{\tilde{x}_T(f_T)} \left( \frac{\tilde{d}_{\text{err}}(f_1^{\text{pc}})}{\tilde{x}_{\text{pc}}(f_1^{\text{pc}})} \right)^{-1} \cdot \frac{\tilde{R}^{\text{static}}(f_T)}{\tilde{R}^{\text{static}}(f_1^{\text{pc}})}, \quad (\text{A7})$$

where  $\tilde{R}(f)$  is the response function, given by

$$\tilde{R}(f) = \frac{1 + \tilde{A}(f) \tilde{D} \tilde{C}(f)}{\tilde{C}(f)}. \quad (\text{A8})$$

In Eq. (A7), we have treated the ratio of the denominators of Eqs. (A5) and (A6) as being constant in time, an approximation that depends on the line frequencies  $f_1^{\text{pc}}$  and  $f_T$  being close together.  $\tilde{d}_{\text{err}}(f_T)$ ,  $\tilde{x}_T(f_T)$ ,  $\tilde{d}_{\text{err}}(f_1^{\text{pc}})$ , and  $\tilde{x}_{\text{pc}}(f_1^{\text{pc}})$  are constantly measured by the calibration pipelines, while the complex constant  $\tilde{R}^{\text{static}}(f_T) / (\tilde{A}_T(f_T) \tilde{R}^{\text{static}}(f_1^{\text{pc}}))$  depends only on static functions at the line frequencies obtained from measurements, and is therefore read into the calibration pipelines, along with several other constants used in computing the TDCFs.

A similar method is used to compute  $\kappa_{\text{PU}}$  with the DARM line  $f_{\text{ctrl}}$  and the same photon calibrator line  $f_2^{\text{pc}}$ , yielding the result

$$\kappa_{\text{PU}} \approx -\frac{1}{\tilde{A}_{\text{PU}}(f_{\text{ctrl}})} \left[ \frac{\tilde{d}_{\text{err}}(f_{\text{ctrl}})}{\tilde{x}_{\text{ctrl}}(f_{\text{ctrl}})} \left( \frac{\tilde{d}_{\text{err}}(f_2^{\text{pc}})}{\tilde{x}_{\text{pc}}(f_2^{\text{pc}})} \right)^{-1} \cdot \frac{\tilde{R}^{\text{static}}(f_{\text{ctrl}})}{\tilde{R}^{\text{static}}(f_2^{\text{pc}})} \right. \right. \\ \left. \left. + \kappa_T \tilde{A}_T(f_{\text{ctrl}}) \right] \right]. \quad (\text{A9})$$

As seen in Eq. (A9),  $\kappa_{\text{PU}}$  depends on  $\kappa_T$ , which is computed first. The optical gain correction factor  $\kappa_C$  and the cavity pole  $f_{\text{cc}}$  depend on both  $\kappa_T$  and  $\kappa_{\text{PU}}$  under this formalism. To measure them, we make use of a higher calibration line injected with the photon calibrator,  $f_4^{\text{pc}} \sim 330$  Hz, where the first term in the denominator of Equation A3 dominates. Solving for  $S(f_4^{\text{pc}})$ , we have

$$S(f_4^{\text{pc}}) = \frac{1}{\tilde{C}_{\text{res}}} \left( \frac{\tilde{x}_{\text{pc}}}{\tilde{d}_{\text{err}}} - \tilde{D} [\kappa_T \tilde{A}_T + \kappa_{\text{PU}} \tilde{A}_{\text{PU}}] \right)^{-1} \Big|_{f_4^{\text{pc}}}. \quad (\text{A10})$$

Then the expressions for  $\kappa_C$  and  $f_{\text{cc}}$  are simply

$$\kappa_C = \frac{|S(f_4^{\text{pc}})|^2}{\Re [S(f_4^{\text{pc}})]}, \quad (\text{A11})$$

$$f_{\text{cc}} = -\frac{\Re [S(f_4^{\text{pc}})]}{\Im [S(f_4^{\text{pc}})]} f_4^{\text{pc}}. \quad (\text{A12})$$

In order to compute the optical spring frequency  $f_s$  and quality factor  $Q$  of the signal recycling cavity (SRC), we need to consider the full model of the sensing function described in Eq. (9). In a similar fashion to the derivation above, we express  $d_{\text{err}}$  in terms of the injected excitations and the TDCFs, this time including the full sensing function model:

$$\begin{aligned}\tilde{d}_{\text{err}} &= \frac{f^2}{f^2 + f_s^2 - i f f_s / Q} \frac{\kappa_C \tilde{C}_{\text{res}}}{1 + i f / f_{\text{cc}}} (\tilde{\Delta L}_{\text{free}} + \tilde{x}_{\text{pc}} - \tilde{\Delta L}_{\text{ctrl}}) \\ &= \frac{\tilde{\Delta L}_{\text{free}} + \tilde{x}_{\text{pc}} - \kappa_T \tilde{A}_T (\tilde{x}_{\text{ctrl}} - \tilde{x}_T) - \kappa_{\text{PU}} \tilde{A}_{\text{PU}} \tilde{x}_{\text{ctrl}}}{(1 + \xi) (S \tilde{C}_{\text{res}})^{-1} + (\kappa_T \tilde{A}_T + \kappa_{\text{PU}} \tilde{A}_{\text{PU}}) \tilde{D}}, \quad (\text{A13})\end{aligned}$$

where we have defined

$$\xi \equiv \frac{f_s^2 - i f f_s / Q}{f^2} \quad (\text{A14})$$

and again used Eq. (A2) to substitute for  $\tilde{\Delta L}_{\text{ctrl}}$ . Demodulating  $d_{\text{err}}$  at the lowest photon calibrator line ( $f_4^{\text{pc}} = 7.93$  Hz at LHO) yields the expression

$$\tilde{d}_{\text{err}}(f_4^{\text{pc}}) = \frac{\tilde{x}_{\text{pc}}}{(1 + \xi) (S \tilde{C}_{\text{res}})^{-1} + (\kappa_T \tilde{A}_T + \kappa_{\text{PU}} \tilde{A}_{\text{PU}}) \tilde{D}} \Big|_{f_4^{\text{pc}}}. \quad (\text{A15})$$

Therefore,  $\xi(f_4^{\text{pc}})$  can be computed in the `gstlal` calibration pipeline using

$$\xi(f_4^{\text{pc}}) = -1 + \left[ S \tilde{C}_{\text{res}} \left( \frac{\tilde{x}_{\text{pc}}}{\tilde{d}_{\text{err}}} - (\kappa_T \tilde{A}_T + \kappa_{\text{PU}} \tilde{A}_{\text{PU}}) \tilde{D} \right) \right]_{f_4^{\text{pc}}}, \quad (\text{A16})$$

and  $f_s$  and  $Q$  take the simple form

$$f_s = f_4^{\text{pc}} \sqrt{\Re[\xi(f_4^{\text{pc}})]}, \quad (\text{A17a})$$

$$Q = -\frac{\sqrt{\Re[\xi(f_4^{\text{pc}})]}}{\Im[\xi(f_4^{\text{pc}})]}. \quad (\text{A17b})$$

Note that the calculation of  $f_s$  and  $Q$  depends on the other TDCFs, which are computed first. Here, we have assumed that the effect of SRC detuning is very small at the higher frequencies used to compute  $\kappa_T$ ,  $\kappa_{\text{PU}}$ ,  $\kappa_C$ , and  $f_{\text{cc}}$ . This is valid as long as  $f_s$  is small compared to those frequencies. We have not neglected the effect of the previously computed TDCFs on  $f_s$  and  $Q$ , as the optical gain and actuation strength clearly have significant contributions here.

## Appendix B: Smoothing of Calibration Factors

As noted in Section III B 3, the computed TDCFs cannot be applied to  $h(t)$  directly due to both excessive noise and the fact that the measurements of the calibration lines are inaccurate when detector noise increases. Here, we describe the method used to attenuate noise in the TDCFs and to discriminate between times of acceptable and unacceptable measurements.

The first step is to accept or reject computed TDCFs based on the coherence between the injection channels  $x_i$  and error signal  $d_{\text{err}}$  at the calibration line frequencies. To compute the coherence between two signals  $x(t)$  and  $y(t)$  at a frequency  $f$ , the signals are demodulated at the chosen frequency using a local oscillator. Then, the coherence is computed as

$$\gamma_{xy}^2(f) = \frac{|\langle \tilde{x}^*(f) \tilde{y}(f) \rangle|^2}{\langle |\tilde{x}(f)|^2 \rangle \langle |\tilde{y}(f)|^2 \rangle}, \quad (\text{B1})$$

where the angled brackets denote averages (actually computed using a low-pass filter) and the superscript asterisk denotes complex conjugation. Coherences are computed using 10-second chunks of input data, and  $n_d = 13$  independent, consecutive values are then averaged, so that each averaged coherence is based on 130 seconds of input data. The average coherence is used to compute the normalized random error in the magnitude of the transfer function  $\hat{H}_{xy}$  at each calibration line frequency:

$$\epsilon \left[ \left| \hat{H}_{xy} \right| \right] \approx \sqrt{\frac{1 - \gamma_{xy}^2}{2 n_d \gamma_{xy}^2}} \quad (\text{B2})$$

as derived in [43]. This uncertainty is computed in the front end and read into the `gstlal` calibration pipeline. If the estimated uncertainty is below the chosen threshold (currently 0.004 at LHO and 0.02 at LLO), a computed TDCF is accepted and passed downstream; otherwise, it is flagged as a gap. Each TDCF is accepted or rejected based on the estimated uncertainty at the frequency of every calibration line used in its computation.

The accepted values are then passed to a 128 s running median, where each new value replaces the oldest value currently in the median array. If computed values are being rejected due to unacceptable coherence, the algorithm will recognize the gap flag associated with those values and instead replace the oldest value in the array with the previously computed median. Thus, when detector noise increases, the reported TDCFs stabilize at the most recent median value computed during the low-noise state. The choice to use a running median instead of, e.g., a running average, is intended to make the result insensitive to occasional outliers that occur in the computed TDCFs, resulting in a smoother time series. The drawback is that computing a median over 128 s of data can be computationally expensive. To offset this extra cost, we have taken advantage of the fact that, in a running median, the previous median is known. This can be used to reduce the number of operations from  $\mathcal{O}(\ell^2)$  to  $\mathcal{O}(\ell)$ , where  $\ell$  is the length of the median array.

A short, 10 second running average is used after the running median in order to remove “kinks” left after the running median. This is computationally cheap and reduces the high-frequency content of the smooth TDCF time series.

All of the gating and smoothing operations are carried out at 16 Hz, before the TDCFs are upsampled to 16 384 Hz and used to correct  $h(t)$ .

TABLE III. A summary of the meaning of each bit in the calibration state vector.

bit	Short descriptor	Long descriptor
0	HOFT_OK	$h(t)$ was successfully computed (logical AND of bits 2-4, 11, 13, 17, and 25)
1	OBS_INTENT	interferometer is in “observation intent” mode
2	OBS_READY	interferometer is in “observation ready” mode
3	HOFT_PROD	$h(t)$ was produced
4	FILTERS_OK	calibration filters settled in
5	NO_STOCH_HW_INJ	No stochastic hardware injections present
6	NO_CBC_HW_INJ	No compact binary coalescence hardware injections present
7	NO_BURST_HW_INJ	No burst hardware injections present
8	NO_DETECTCHAR_HW_INJ	No detector characterization hardware injections present
9	NO_GAP	The input data was present (not a gap)
10	KAPPA_SMOOTHING_OK	TDCFs smoothing algorithm is settled in
11	KAPPA_TST_SMOOTH.OK	Smoothed $\kappa_T$ output is in expected range
12	KAPPA_TST_MEDIAN.OK	Median array used for $\kappa_T$ smoothing not dominated by bad coherence time
13	KAPPA_PU_SMOOTH.OK	Smoothed $\kappa_{PU}$ output is in expected range
14	KAPPA_PU_MEDIAN.OK	Median array used for $\kappa_{PU}$ smoothing not dominated by bad coherence time
15	not in use	not in use
16	not in use	not in use
17	KAPPA_C_SMOOTH.OK	Smoothed $\kappa_C$ output is in expected range
18	KAPPA_C_MEDIAN.OK	Median array used for $\kappa_C$ smoothing not dominated by bad coherence time
19	F_CC_SMOOTH.OK	Smoothed $f_{cc}$ output is in expected range
20	F_CC_MEDIAN.OK	Median array used for $f_{cc}$ smoothing not dominated by bad coherence time
21	SUS_COH.OK	Coherence uncertainty for SUS calibration line is acceptable
22	DARM_COH.OK	Coherence for DARM calibration line is acceptable
23	PCALY_LINE1_COH.OK	Coherence for first PCAL line is acceptable
24	PCALY_LINE2_COH.OK	Coherence for second PCAL line is acceptable
25	NO_UNDERFLOW_INPUT	Magnitude of input for all channels is between $1 \times 10^{-35}$ and $1 \times 10^{35}$
26	F_S_SMOOTH.OK	Smoothed $f_s$ output is in expected range
27	F_S_MEDIAN.OK	Median array used for $f_s$ smoothing is not dominated by bad coherence time
28	Q_SMOOTH.OK	Smoothed $Q$ of SRC output is in expected range
29	Q_MEDIAN.OK	Median array used for $Q$ of SRC smoothing is not dominated by bad coherence time

### Appendix C: Calibration State Vector

The `gstlal` calibration pipeline computes a bitwise state vector that summarizes the integrity of the calibration at a sample rate of 16 Hz. The bit definition of the calibration state vector in Advanced LIGO’s second observing run is shown in Table III. A value of zero for a bit means the bit is False and a value of 1 means the bit is True.

The zeroth bit of the state vector indicates that  $h(t)$  is considered valid and usable for astrophysical analyses. Bit 1 in the state vector is determined based on state information provided by the operator and the front-end system. If bit 1 is set to True, then the operator has determined that no commissioning activities are ongoing and science-quality data should be available. Similarly, bit 2 is determined based on state information provided by the front-end system and indicates that the IFO has reached a nominal low-noise configuration. Bit 3 indicates whether or not strain was computed by the pipeline, but this bit does not necessarily indicate the validity of the strain data at that time.

Bit 4 indicates whether the various FIR filters have settled in since the IFO reached a nominal low-noise state as determined by bit 2. This bit will be turned off for  $N$  seconds after the observation-ready state is reached and will also be turned off for  $N$  seconds before the observation-ready state is lost, where

$N$  seconds is the total filter settle time for all FIR filters in the pipeline. This is due to the artificial delay and then compensated advance in the FIR filters, as discussed in Sec. III B 1.

Bits 5-8 indicate whether any known hardware injections are present in the data. A hardware injection is when the end test masses of the interferometer are actuated to mimic an astrophysical signal [44]. Hardware injections are performed for astrophysical sources ranging from compact binary mergers to continuous GW emission as from an isolated, rotating neutron star. Bit 9 indicates whether there are times that no input data was received by the calibration pipeline. Bits 10-24 and 26-29 are all associated with the TDCFs calculation and its smoothing process (see Appendix A). In particular, bits 11, 13, and 17 indicate whether or not the computed TDCFs that are used to correct  $h(t)$  ( $\kappa_C$ ,  $\kappa_{PU}$ , and  $\kappa_T$ ) are within some expected range of values. If the TDCFs stray outside of the expected range, this is a red flag that something about the current reference calibration model may now be drastically inaccurate. Bit 25 indicates whether the input could have caused arithmetic underflows or overflows.

Consumers of the  $h(t)$  data product are advised to use the logical AND of bits 0 and 1 to determine whether to analyze data for astrophysical signals. Bit 0 indicates the overall integrity of the  $h(t)$  calculation while bit 1 indicates that the operator has determined the interferometer is in trustworthy, science-quality data-taking state.

---

[1] B. P. Abbott *et al.* (LIGO Scientific Collaboration and Virgo Collaboration), *Phys. Rev. Lett.* **116**, 061102 (2016).

[2] B. P. Abbott *et al.* (LIGO Scientific Collaboration and Virgo Collaboration), *Phys. Rev. Lett.* **116**, 241103 (2016).

[3] B. P. Abbott *et al.* (LIGO Scientific Collaboration and Virgo Collaboration), *Phys. Rev. X* **6**, 041015 (2016).

[4] B. P. Abbott *et al.* (LIGO Scientific Collaboration and Virgo Collaboration), *Phys. Rev. Lett.* **118**, 221101 (2017).

[5] B. P. Abbott, R. Abbott, T. D. Abbott, F. Acernese, K. Ackley, C. Adams, T. Adams, P. Addesso, R. X. Adhikari, and et al. (LIGO Scientific Collaboration and Virgo Collaboration), *Phys. Rev. Lett.* **119**, 141101 (2017).

[6] B. P. Abbott, R. Abbott, T. D. Abbott, F. Acernese, K. Ackley, C. Adams, T. Adams, P. Addesso, R. X. Adhikari, and et al. (LIGO Scientific Collaboration and Virgo Collaboration), *Phys. Rev. Lett.* **119**, 161101 (2017).

[7] B. P. Abbott *et al.* (LIGO Scientific Collaboration), *Phys. Rev. D* **95**, 062003 (2017).

[8] K. Izumi and D. Sigg, *Classical Quant. Grav.* **34**, 015001 (2016).

[9] B. P. Abbott *et al.* (LIGO Scientific Collaboration and Virgo Collaboration), *Phys. Rev. Lett.* **116**, 131103 (2016).

[10] J. Aasi *et al.*, *Classical Quant. Grav.* **32**, 074001 (2015).

[11] A. Buonanno and Y. Chen, *Phys. Rev. D* **65**, 042001 (2002).

[12] X. Siemens *et al.*, *Class. Quant. Grav.* **21**, S1723 (2004).

[13] C. Cahillane, J. Betzwieser, D. Brown, E. Goetz, E. D. Hall, K. Izumi, S. Kandhasamy, S. Karki, J. S. Kissel, G. Mendell, R. L. Savage, D. Tuyenbayev, A. Urban, A. Viets, M. Wade, and A. J. Weinstein, ArXiv e-prints (2017), [arXiv:1708.03023](https://arxiv.org/abs/1708.03023) [astro-ph.IM].

[14] D. Tuyenbayev *et al.*, *Classical Quant. Grav.* **34**, 015002 (2016).

[15] D. V. Martynov *et al.*, *Phys. Rev. D* , 112004 (2016).

[16] S. Karki *et al.*, *Rev. Sci. Instrum.* **87**, 114503 (2016).

[17] N. A. Robertson *et al.*, *Classical Quant. Grav.* **19**, 4043 (2002).

[18] S. M. Aston *et al.*, *Classical Quant. Grav.* **29**, 235004 (2012).

[19] L. Carbone *et al.*, *Classical Quant. Grav.* **29**, 115005 (2012).

[20] F. Matichard *et al.*, *Precision Engineering* **40**, 273 (2015).

[21] B. P. Abbott *et al.*, *Astrophys. J. Lett.* **833**, L1 (2016).

[22] B. P. Abbott *et al.* (LIGO Scientific Collaboration and Virgo Collaboration), *Phys. Rev. Lett.* **118**, 121101 (2017).

[23] B. P. Abbott *et al.* (LIGO Scientific Collaboration and Virgo Collaboration), *Phys. Rev. Lett.* **118**, 121102 (2017).

[24] B. P. Abbott *et al.*, *The Astrophysical Journal* **839**, 12 (2017).

[25] B. P. Abbott *et al.*, *in prep* (2017).

[26] N. Yunes, K. Yagi, and F. Pretorius, *Phys. Rev. D* **94**, 084002 (2016).

[27] K. Chamberlain and N. Yunes, [arXiv preprint arXiv:1704.08268](https://arxiv.org/abs/1704.08268) (2017).

[28] B. P. Abbott *et al.* (LIGO Scientific and Virgo Collaborations), *Phys. Rev. Lett.* **116**, 221101 (2016).

[29] D. F. Chernoff and L. S. Finn, *Astrophys. J.* **411**, L5 (1993).

[30] B. P. Abbott *et al.* (LIGO Scientific Collaboration and Virgo Collaboration), *Phys. Rev. Lett.* **116**, 241102 (2016).

[31] L. P. Singer *et al.*, *Astrophys. J.* **795**, 105 (2014), [arXiv:1404.5623](https://arxiv.org/abs/1404.5623) [astro-ph.HE].

[32] “GStreamer,” <https://gstreamer.freedesktop.org/>.

[33] “LAL,” <https://wiki.ligo.org/DASWG/LALSuite>.

[34] “gstlal,” <https://wiki.ligo.org/DASWG/GstLAL>.

[35] “MATLAB c2d,” <https://www.mathworks.com/help/control/ref/c2d.html>.

[36] “MATLAB minreal,” <https://www.mathworks.com/help/control/ref/minreal.html>.

[37] T. Laakso and V. Valimaki, *IEEE Signal Processing* **13**, 30 (1996).

[38] “gstlal-calibration,” <https://versions.ligo.org/cgit/gstlal/tree/gstlal-calibration?h=gstlal-calibration-1.1.7-v1>.

[39] “MATLAB,” <https://www.mathworks.com/help/matlab/>.

[40] “GStreamer audioresampler,” <https://gstreamer.freedesktop.org/data/doc/gstreamer/head/gst-plugins-base-plugins/html/gst-plugins-base-plugins-audioresample.html>.

[41] “LIGO data grid,” <https://wiki.ligo.org/LDG/>.

[42] J. Abadie *et al.* (VIRGO, LIGO Scientific), (2012), [arXiv:1203.2674](https://arxiv.org/abs/1203.2674) [gr-qc].

[43] J. S. Bendat and A. G. Piersol, *Random data: analysis and measurement procedures*, Vol. 729 (John Wiley & Sons, 2011).

[44] C. Biwer *et al.*, *Phys. Rev.* **D95**, 062002 (2017), [arXiv:1612.07864](https://arxiv.org/abs/1612.07864) [astro-ph.IM].